Identification of an Electric UAV Propulsion System in Icing Conditions

Bogdan Løw-Hansen, Nicolas C. Müller
Department of Engineering Cybernetics, NTNU, Trondheim, Norway

Erlend M. Coates
Department of ICT and Natural Sciences, NTNU, Ålesund, Norway

Tor Arne Johansen, Richard Hann
Department of Engineering Cybernetics, NTNU, Trondheim, Norway

Abstract

In-flight atmospheric icing is a severe hazard for propeller-driven unmanned aerial vehicles (UAVs) that can lead to issues ranging from reduced flight performance to unacceptable loss of lift and control. To address this challenge, a physics-based first principles model of an electric UAV propulsion system is developed and identified in varying icing conditions. Specifically, a brushless direct current motor (BLDC) based propeller system, typical for UAVs with a wing span of 1-3 meters, is tested in an icing wind tunnel with three accreted ice shapes of increasing size. The results are analyzed to identify the dynamics of the electrical, mechanical, and aerodynamic subsystems of the propulsion system. Moreover, the parameters of the identified models are presented, making it possible to analyze their sensitivity to ice accretion on the propeller blades. The experiment data analysis shows that the propeller power efficiency is highly sensitive to icing, with a 40% reduction in thrust and a 16% increase in torque observed on average across the tested motor speeds and airspeeds. The resulting reduction in propeller efficiency can be as high as 70% in the worst-case scenario. These findings provide valuable insights into the impact of ice accretion on electric propeller systems and contribute to the development of effective ice protection systems for safer UAV operation in cold environments.

Nomenclature

v	phase voltage	V
$v_{l\text{-}l}$	line-to-line voltage	V
v_n	neutral point voltage	V
n	circuit neutral point	
v_0	ESC voltage drop	V
v_b	supply DC voltage	V
i_b	supply DC current	A
i_0	zero-load current	A
v_1, v_2, v_3	armature coil voltage	V
i_1, i_2, i_3	armature coil current	A
R	equivalent circuit resistance	Ω
L	equivalent circuit inductance	H
k_E	equivalent circuit back-emf constnat	$\mathrm{V}/(\mathrm{rad/s})$
k_V	electric motor speed constant	RPM / V
$R_{l\text{-}l}$	line-to-line resistance	Ω
R_1, R_2, R_3	armature coil resistance	Ω
L_1, L_2, L_3	armature coil inductance	H
$k_{E,1}, k_{E,2}, k_{E,3}$	armature coil back-emf constant	$\mathrm{V}/(\mathrm{rad/s})$
δ_t	normalized PWM input $\in [0, 1]$	(-)
$F_{\text{ESC}}(\delta_t)$	ESC voltage transmission function $\in [0, 1]$	(-)
p_0, p_1, p_2	F_{ESC} model parameters	(-)
t	time	s
ω	motor shaft velocity	$\mathrm{rad/s}$
$\dot{\omega}$	motor shaft acceleration	$\mathrm{rad/s^2}$
I	motor intertia	$\mathrm{kg\,m^2}$
ρ	air density	$\mathrm{kg/m^3}$
D	propeller diameter	m
S_p	area swept by the propeller	$\mathrm{m^2}$
V_a	airspeed	m/s
V_e	propeller air exit speed	m/s
k_m	throttle-based thrust constant	m/s
k_{mq}	throttle-based torque constant	$\mathrm{kg\,m^2/rad^2}$
k_ω	throttle-based motor speed constant	$\mathrm{rad/s}$
k_Q	electric torque constant	$\mathrm{N\,m/A}$
T	propeller thrust	N
Q	propeller torque	$\mathrm{N\,m}$
J	advance ratio	(-)
e_p	model parameter for propeller efficiency	(-)
η_p	computed propeller efficiency factor	(-)
C_Q	nondimensionalized torque	(-)
C_T	nondimensionalized thrust	(-)
$C_{q_0}, C_{q_1}, C_{q_2}$	nondimensionalized torque coefficients	
$C_{t_0}, C_{t_1}, C_{t_2}$	nondimensionalized thrust coefficients	
y	model response variable	
z	measured response variable	
ν	measurement error	
$\bar{z}$	averaged response variable	
θ	model parameter	
$\boldsymbol{\xi}$	regressor vector	
$\boldsymbol{X}$	regressor matrix	
N	number of measured samples	
n_p	number of estimated model parameters	
j	parameter index	
$s(\hat{\theta})$	standard error	
R^2	model fit analysis metric	
SS_R, SS_E, SS_T	sum of squared errors	
BM	subscript for Beard & McLain thrust model	
$clean$	subscript for ice-free model parameter	
$measured$	subscript for measured data	
$\hat{}$	symbol for estimated variable or parameter	
bold symbol	vector form	

Introduction

Application of small electrically-propelled fixed-wing unmanned aerial vehicles (UAVs) has increased rapidly in the last decade, covering a range of use cases such as mapping, surveillance, package delivery, and warfare [1]. The main factors that have enabled such rapid adoption are access to relatively cheap, lightweight, and efficient subsystems, including autopilot hardware based on micro-electromechanical system (MEMS) sensors [2], improved communication technology, and electric propulsion systems.

The increased commercial and military utilization of UAVs has resulted in higher expectations towards the operability of such aircraft in all weather conditions [1], including heavy wind, rain, snow, and icing [3]. Among the harsh weather conditions, icing is considered the most challenging and hazardous [4].

One approach to enabling the use of UAVs in icing conditions is to use modeling and system identification to develop an understanding of the effect ice accretion has on the UAV's performance. Given a performance degradation model, it is possible to develop performance-based icing detection algorithms and implement control strategies to mitigate the adverse effects of icing on vehicle dynamics [5, 6]. In addition, having access to a model that can describe the impact of icing on the UAV's dynamics allows the UAV to be operated closer to its maximal potential and enables safer autonomous flights.

Several studies on the general modeling of electric UAV propulsion systems in nominal conditions, i.e., not icing conditions, can be found in recent literature. For instance, Coates et al. [7] performed system identification using wind tunnel tests and compared a physics-based propulsion system model with two throttle-based thrust models. Similarly, a multi-physical model of a brushless direct current (BLDC) motor is identified by Michel et al. [8] to analyze the energy dynamics of a multirotor UAV in nominal operating conditions.

In literature from the early 2000s, modeling, and identification of three-phase BLDC motors, not necessarily used for UAV propulsion, can be found. For instance, Moseler and Isermann [9] develop a model-based fault detection algorithm for a three-phase BLDC motor. Their paper discusses assumptions and simplifications necessary for developing a linear BLDC motor model. Some of their notation is adopted in this paper. More recently, a frequency domain approach to the system identification of a BLDC motor has been presented by Xiang et al. [10].

Analysis of propeller system degradation has recently gained attention due to the increased commercial interest in battery-powered UAVs. Early experimental analysis of UAV propeller and performance degradation due to icing was conducted by Liu et al. [11, 12] in 2018, and several newer publications on propeller performance analysis in icing conditions can be found in [13, 14, 15, 16, 17]. In addition to experimental studies, some simulation-based analysis using icing CFD tools has been presented by Ozcer et al. [18] and by Müller et al. [19], where the first article describes ice accretion on aircraft in general, while the latter focuses on UAV propeller icing.

Although there is a growing amount of literature analyzing the penalties related to the operation of UAV propeller systems in icing conditions, only a few researchers have attempted to identify a model capable of predicting propeller performance at different icing severity levels. Such a model can potentially allow for the development of an icing severity detection algorithm based on, for example, fault detection filters (FDF) [20] — a model-based approach to fault detection that has been developed and improved by the automatic control research community since the 1960s.

Some relevant work on the development of ice detection algorithms for propeller-based systems is presented by Haaland et al. in [21] where a multiple model estimation (MME) is used to predict the icing severity of a propeller system. A more comprehensive work is presented by McKillip et al. in [6], where the authors use icing computational fluid dynamics (CFD) results and icing wind tunnel (IWT) experiments to analyze the propulsion system of an electric vertical take-off and landing vehicle in icing conditions and develop an FDF algorithm for in-flight icing detection. The results in [21, 6] show the importance of having a model of the propulsion system when developing an algorithm for the detection of in-flight icing.

Having a model of the propulsion system and understanding how it changes due to icing can lead to several important benefits. These benefits include the possibility of implementing FDFs, simulating the propulsion system, and for instance, determining the effect of an iced propeller on the overall flight mission. Additionally, it allows quantifying the cost of flying with degraded performance versus using a de-icing system — information that can greatly benefit the work similar to Wallisch et al. [22]. Motivated by the aforementioned benefits of having a propulsion system model, this paper presents the results of UAV propeller system modeling in nominal and iced conditions. In particular, the modeling results were achieved using experimental data gathered at four icing severity conditions based on the icing exposure time, namely: 0, 20, 40, and 60 seconds. The exposure times were limited by the substantial ice shedding observed for ice shapes accreted for more than 60 s and the fact that significant performance degradation could be observed already after 20 seconds of in-flight icing.

The experiments in this study are documented by a comprehensive set of measurements, including power supply voltage and current, the motor phase voltage, motor shaft velocity, and propeller torque and thrust forces. Access to these measurements has allowed the identification of a multi-system model comprising the electric, mechanical, and aerodynamic subsystems of a UAV propulsion system at three different icing severity levels — a result that has not been observed in the available literature. The goal of modeling the UAV propulsion system in this way is to highlight the sensitivity of various model parameters and variables to icing severity, thus making it easier to develop model-based ice detection algorithms for UAVs.

Prior to the experiment design, a hypothesis was made to describe the expected outcome of this study. The hypothesis relates to which parts of an electric propulsion system change due to ice accretion on the propeller blades. Specifically, it was theorized that the accreted ice mainly affects the aerodynamic properties of the propeller by changing its geometrical shape. In terms of performance, this translates to increased drag and torque and reduced lift and thrust produced by the propulsion system. In contrast, the electro-mechanical subsystems that describe the conversion of power from electric to mechanical are expected to stay unaffected. The findings of this study are analyzed and compared to the stated hypothesis in section Results.

Methods

This section presents the theory for modeling and identification of an electric propeller-based system in nominal and iced conditions.

Electrical System

In the studied propulsion system, when a throttle command is sent in the form of a pulse-width modulated (PWM) signal, the first components it reaches are the electronic speed controller (ESC) and the BLDC motor. The task of the ESC in this set-up is to convert the

DC voltage from a power supply into a PWM-modulated voltage that can generate torque by timely switching the current flow in the armature coils of the motor. The electric switches are usually connected in a bridge structure as shown in Fig. 1, where v_b and i_b are the power supply voltage and current, v_1, v_2, v_3 and i_1, i_2, i_3 are the three motor armature coil voltages and currents, and PWM is the throttle signal.

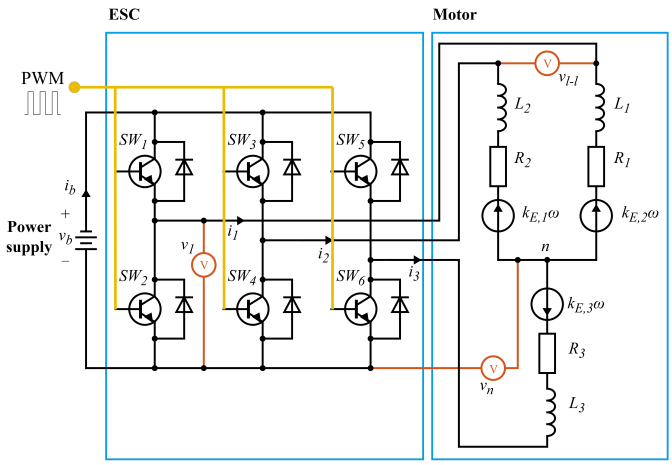

Figure 1: ESC and BLDC motor circuit. Electric switches are labeled SW. The red lines show the voltmeter connection points necessary to measure the line-to-line voltage $v_{l\text{-}l}$, the armature voltage v_1, and the neutral point voltage v_n. The yellow line indicates where the PWM signal enters the switches.

The bridge circuits of the type shown in Fig. 1 are nonlinear, complex, and non-trivial to analyze. It is, therefore, common to work with equivalent circuits when analyzing and modeling the combined ESC and BLDC motor dynamics [7, 9]. Following [7, 9], the equivalent circuit is set up according to Fig. 2, where i and v are the average phase current and phase voltage supplied to the motor.

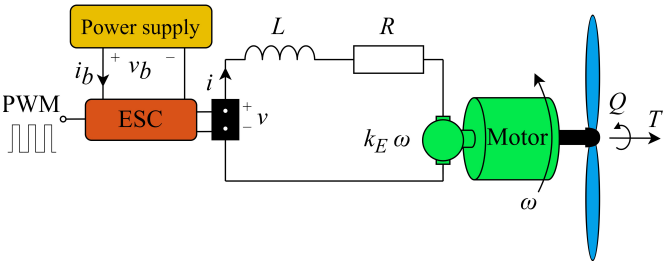

Figure 2: Equivalent circuit showing the propulsion system from PWM throttle input to propeller thrust T and torque Q.

According to [9], the voltage balance over the equivalent circuit can be formulated as follows,

$$v\,(t) = Ri\,(t) + L\frac{d}{dt}i\,(t) + k_E\omega\,(t) \tag{1}$$

where t is time, and the current i, voltage v, and motor shaft speed ω are related through the coupled resistance R, inductance L, and back-EMF constant k_E, which are calculated based on the individual armature coil coefficients, shown in Fig. 1:

$$R = \frac{2}{3}\,(R_1 + R_2 + R_3) \tag{2}$$

$$L = \frac{2}{3}\,(L_1 + L_2 + L_3) \tag{3}$$

$$k_E = \frac{2}{3}\,(k_{E,1} + k_{E,2} + k_{E,3}) \tag{4}$$

In Eqs. 2–4, the factor of two is related to the fact that the power balance is calculated over two of the armature coils at each instance.

The BLDC Motor Model

Equation 1 describes a model that relates the motor's average phase voltage, phase current, and angular velocity. Usually, the measurements of the motor phase voltage and current are unavailable; therefore, it is useful to describe these values in terms of the PWM throttle signal and the supply voltage v_b and current i_b. This can be achieved through the ESC power balance in Eq. 5, which states that the power on the input and output sides of the ESC must be equal.

$$v_b(t) \cdot i_b\,(t) = v(t) \cdot i(t) \tag{5}$$

Following [8, Eq. 22], the phase voltage in Eq. 5 can be described as a function of the supply voltage, and the normalized PWM throttle signal $\delta_t(t) \in [0, 1]$ as follows,

$$v(t) = F_{\text{ESC}}(\delta_t(t)) \cdot v_b(t) \tag{6}$$

or

$$F_{\text{ESC}}(\delta_t(t)) = \frac{v(t)}{v_b(t)} \tag{7}$$

where $F_{\text{ESC}}(\delta_t(t))$, referred to as the ESC transmission function, is the function that relates the throttle input δ_t to the fraction of the supplied voltage v_b transmitted to the motor. In [7, 8], the ESC transmission function is a linear function of δ_t; however, in this paper, based on power supply voltage and phase voltage measurements, F_{ESC} was determined to be a second-order function of δ_t of the following form,

$$F_{ESC}(\delta_t) = p_0 + p_1 \cdot \delta_t + p_2 \cdot \delta_t^2 \tag{8}$$

Similarly to voltage, the average phase current $i(t)$ can be described as a function of the supply current and the normalized PWM throttle signal. Starting by rearranging, Eq. 5 gives:

$$i\,(t) = \frac{i_b(t)}{v(t)/v_b(t)} \tag{9}$$

then by using $v(t)$ from Eq. 6 the following expression is obtained,

$$i\,(t) = \frac{i_b(t)}{F_{\text{ESC}}(\delta_t(t))} \quad \text{when} \quad F_{\text{ESC}}(\delta_t(t)) \neq 0 \tag{10}$$

resulting in two expressions for the phase current $i(t)$. Although the parameters of the F_{ESC} function in Eq. 8 are identified in this study, since the measurements of both the supply voltage $v_b(t)$ and phase voltage $v(t)$ are available for all experiments, the phase current is always calculated using Eq. 9. The same information is not normally available during the flight. Thus identifying the F_{ESC} function is important for the prediction of the phase voltage when it is not measured, i.e., during flight.

When modeling electromechanical processes, it is common to ignore the dynamics of the electrical system as they are much faster

compared to the mechanical system. For instance, this is true when considering the dynamics of current and angular velocity in a BLDC motor. As such, the electric model is simplified by assuming that time derivatives are zero. In Eq. 1, setting $\frac{d}{dt}i = 0$ gives the following steady state voltage balance,

$$v\left(t\right) = Ri\left(t\right) + k_E\omega\left(t\right) \tag{11}$$

Furthermore, when analyzing the combined ESC and motor system, it might be relevant to include a voltage drop v_0 over the ESC,

$$v\left(t\right) = Ri\left(t\right) + k_E\omega\left(t\right) + v_0 \tag{12}$$

When working with real-world systems, one should be aware that the simplified first-order model in Eq. 12 will not be able to capture the system's full complexity. For instance, many ESCs designed for propeller systems use feedback to achieve an exponential throttle-to-motor-shaft-speed relation, which results in a linear throttle-to-thrust relation and makes the throttle input more intuitive for the pilot. However, this unmodelled feedback may introduce significant changes to the system's dynamics, making it nonlinear.

BLDC Motor Parameter Measurements

Measuring the circuit parameters and the signals going through a BLDC motor is not trivial. In a star-connected motor, the measured resistance between two armature wires is the line-to-line resistance, and the phase resistance is then the measured line-to-line resistance divided by two. Given that all three armature resistances are equal, the average resistance in the equivalent circuit is then calculated as,

$$\begin{aligned} R = \frac{2}{3}\cdot 3\cdot R_1 = 2\cdot R_1 = R_{l\text{-}l} \\ \text{when } R_1 = R_2 = R_3 \end{aligned} \tag{13}$$

Voltage measurement can be done using an AC voltmeter using the true-RMS setting. The true RMS setting is essential as the measured value is a noisy PWM-modulated signal far from an ideal sinusoid. In a star-connected motor, the voltage measurement between any two of the three armatures gives the line-to-line voltage $v_{l\text{-}l}$. Furthermore, the line-to-line voltages lead the phase voltages by 30° and thereby are larger by a factor of $\sqrt{3}$,

$$v(t)\sqrt{3} = v_{l\text{-}l}(t) \implies v(t) = \frac{1}{\sqrt{3}}v_{l\text{-}l}(t) \tag{14}$$

Mechanical System

BLDC motors use permanent magnets and switching of the current in the armature coils, i.e., current commutation, to generate torque and drive the mechanical part of the propulsion system. Therefore, in a BLDC motor, the produced torque is directly proportional to the input current, i.e., the average phase current $i(t)$.

The torque balance equation for a BLDC motor can describe in the following way,

$$I\dot{\omega}(t) = k_Q(i(t) - i_0) - Q(t) \tag{15}$$

where I is the rotor and propeller inertia, Q is the load torque, k_Q is the torque constant, and i_0 is the zero load current, which can be viewed as additional internal load caused by friction and other losses. Some articles include viscous friction $c_v\omega(t)$ as part of the torque model; however, based on findings in [7], and initial analysis of experimental data, it has been determined that due to its small size, the viscous friction can be discarded. When analyzing the torque in steady state, i.e., with $\dot{\omega} = 0$, the torque balance can be simplified to the following form,

$$Q(t) = k_Q(i(t) - i_0) \tag{16}$$

Torque and Back-EMF Constants

In a BLDC motor, the stator windings and permanent magnets on the rotor generate a nearly uniform flux density in the air gap between them [23]. The torque constant k_Q $(\mathrm{Nm/A})$ and the back-EMF constant k_E $(\mathrm{V/(rad/s)})$ are both directly related to this magnetic flux density in the motor and represent the conversion rate between electrical and mechanical energy. In theory, both constants should be equal when using SI units, and it is often assumed that $k_Q = k_E$. However, losses associated with converting energy from electrical to mechanical and mechanical to electrical can differ, and slight deviations can be expected.

Aerodynamic System

The aerodynamic subsystem models the thrust T and torque Q produced by the propeller as a function of the propeller's angular velocity, blade geometry, and atmospheric conditions. For easier comparison and analysis of propeller performance, the torque and thrust coefficients are typically nondimensionalized [7]:

$$C_T = \frac{4\pi^2 T}{\rho D^4 \omega^2} \tag{17}$$

$$C_Q = \frac{4\pi^2 Q}{\rho D^5 \omega^2} \tag{18}$$

where ρ is the air density, and D is the propeller diameter.

At low speeds typical for a fixed-wing UAV, the C_T, and C_Q coefficients mainly depend on the advance ratio:

$$J = \frac{2\pi V_a}{\omega D} \tag{19}$$

where V_a is the airspeed. Using dimensional analysis, it has been demonstrated that the thrust and torque coefficients mainly depend on three variables: advance ratio, propeller blade Reynolds number, and propeller tip Mach number [24]. Among these variables, the advance ratio J is the most important term for the thrust and torque models, as also noted in [7, 24]. Therefore, based on initial identification results and to prevent over-parametrization and overfitting of the model, a second-order advance ratio-based polynomial is used to approximate the forces:

$$C_T(J) = C_{t_0} + C_{t_1}J + C_{t_2}J^2 \tag{20}$$

$$C_Q(J) = C_{q_0} + C_{q_1}J + C_{q_2}J^2 \tag{21}$$

giving the following polynomial thrust and torque equations:

$$T = \frac{\rho D^4}{4\pi^2}\left(C_{t_0} + C_{t_1}J + C_{t_2}J^2\right)\omega^2 \tag{22}$$

$$Q = \frac{\rho D^5}{4\pi^2}\left(C_{q_0} + C_{q_1}J + C_{q_2}J^2\right)\omega^2 \tag{23}$$

Throttle-based Thrust and Torque Models

In addition to the physical models described in the previous chapters, several simplified models for calculating thrust based on throttle input have been proposed in the literature. These models are useful since they are easy to implement and do not require extensive modeling of electromechanical propulsion subsystems. Similarly to Coates et al. [7], a throttle-based thrust model is compared to the physics-based model to establish the usefulness and applicability of such models for modeling ice-induced performance degradation. The throttle-based model examined in this study is the Beard & McLain model found in [25, Ch. 4.3] labeled here with the subscript BM.

$$T_{BM} = \frac{1}{2}\rho S_p e_p((k_m\delta_t)^2 - V_a^2) \tag{24}$$

In this throttle-based model, the thrust is calculated based on the throttle input δ_t, the airspeed V_a, the propeller efficiency factor e_p, the motor constant k_m, the air density ρ, and the area swept by the propeller $S_p = \frac{1}{4}\pi D^2$ given by the propeller diameter D.

An equivalent throttle-based torque model is proposed in [25]. The proposed model describes the motor shaft speed as a function of the throttle input times a motor speed constant, $\hat{\omega} = k_\omega \delta_t$, and then models the throttle-based torque as a second-order function of $\hat{\omega}(\delta_t)$, as shown in Eq. 25, where k_{mq} is a model-specific torque constant.

$$Q_{BM} = k_{mq}\hat{\omega}^2 \tag{25}$$

An analysis of Eq. 25 shows that it is equivalent to Eq. 23 if the terms related to airspeed are removed. Due to this reason, and the fact that the motor shaft speed is assumed to be known in most cases, this throttle-based torque model is not further investigated in this study.

System Identification

System identification in this study is performed using the rank-deficient least squares (LS) algorithm. The general LS regression equation can be formulated in the following way,

$$\begin{aligned} \boldsymbol{y} &= \boldsymbol{X\theta} \\ \boldsymbol{z} &= \boldsymbol{X\theta} + \boldsymbol{\nu} \end{aligned} \tag{26}$$

where
$\boldsymbol{y} = [y(1)\ y(2)\ ...\ y(N)]^T = N \times 1$ vector of model response variables,
$\boldsymbol{z} = [z(1)\ z(2)\ ...\ z(N)]^T = N \times 1$ vector of measured response variables,
$\boldsymbol{\theta} = [\theta_0\ \theta_1\ ...\ \theta_j]^T = n_p \times 1$ vector of unknown parameters, $n_p = j + 1$
$\boldsymbol{X} = \left[1\ \boldsymbol{\xi}_1\ ...\ \boldsymbol{\xi}_j\right] = N \times n_p$ matrix given by a column of ones and regressor vectors $\boldsymbol{\xi}$, and
$\boldsymbol{\nu} = [\nu(1)\ \nu(2)\ ...\ \nu(N)]^T = N \times 1$ vector of measurement errors.

For an LS problem stated above, the solution that returns the parameter estimate $\hat{\boldsymbol{\theta}}$ is given by the normal equation,

$$\hat{\boldsymbol{\theta}} = \left(\boldsymbol{X^T X}\right)^{-1} \boldsymbol{X^T z} \tag{27}$$

which can then be used to predict the model response,

$$\hat{\boldsymbol{y}} = \boldsymbol{X}\hat{\boldsymbol{\theta}} \tag{28}$$

In Eq. 27 if the regressor vectors $\boldsymbol{\xi}_k\ ,\ k \in (1, .., j)$ in $\boldsymbol{X}$ are linearly independent, then $\boldsymbol{X^T X}$ is positive definite, and $\left(\boldsymbol{X^T X}\right)^{-1}$ exists. However, in many regression problems, due to model over-parametrization and insufficient excitation in the dataset, the regressors are often dependent and colinear, leading to sensitivity when using $\left(\boldsymbol{X^T X}\right)^{-1}$. Several methods have been developed to deal with this problem. One such method is the rank-deficient LS algorithm described in [26, Ch. 6.3.2]. This particular LS method uses singular value decomposition (SVD) and an elimination step to remove near singular values from the SVD decomposition to perform robust matrix inverse operations. The elimination step is essential to computing a robust inverse when the information matrix has near-singular eigenvalues caused by near-linear dependencies among the regressors. In this study, the rank-deficient SVD-based LS regression has been used for some of the identification problems. The use of the rank-deficient LS algorithm is stated where applicable. This is important as using the reduced SVD solution in regression results in invalid parameter uncertainties, and thus the metrics such as the stand error in Eq. 32 cannot be used to describe the true uncertainty of the identified parameters.

Error Analysis Metrics

Comparing system identification results can be challenging; it is, therefore, beneficial to use several metrics to assess the fitness of a model and its parameters. Based on [26, 24], the following metrics have been chosen: the R^2, the root mean square error (RMSE), and the standard error.

$\mathbf{R^2}$

The R^2 metric is based on partitioning the model prediction error into the regression sum of squares SS_R and the residual sum of squares SS_E. This partitioning makes it possible to characterize the variation of the response variable about its mean,

$$\begin{aligned} SS_R &\equiv \sum_{i=1}^{N} \left(\hat{y}(i) - \bar{z}\right)^2 \quad , \quad \bar{z} = \frac{1}{N}\sum_{i=1}^{N} z(i) \\ SS_E &\equiv \sum_{i=1}^{N} \left(z(i) - \hat{y}(i)\right)^2 \\ SS_T &= SS_R + SS_E \end{aligned} \tag{29}$$

Using the definitions in Eq. 29, the R^2 metric can be defined as function of the unexplained error SS_E and the total error SS_T,

$$\mathsf{R}^2 = 1 - \frac{SS_E}{SS_T} \tag{30}$$

Root Mean Square Error

The RMSE is given by the square root of the normalized residual sum of squares,

$$\text{RMSE} = \sqrt{\frac{1}{N}\sum_{i=1}^{N} \left(z(i) - \hat{y}(i)\right)^2} = \sqrt{\frac{SS_E}{N}} \tag{31}$$

Standard Error

The standard error is a useful metric for analyzing the fitness of each individual parameter estimate. It is important to note that the standard error calculation assumes uncorrelated measurement errors and a sufficiently correct model structure. Thus, this metric is less useful when the modeling error is large. The vector of standard errors $\boldsymbol{s}(\hat{\boldsymbol{\theta}})$ corresponding to the estimated parameters $\hat{\boldsymbol{\theta}}$ is given as

$$\boldsymbol{s}(\hat{\boldsymbol{\theta}}) = \sqrt{\left[\frac{SS_E}{N - n_p}\right] \cdot \mathtt{diag}[\left(\boldsymbol{X^T X}\right)^{-1}]} \tag{32}$$

The standard error can also be expressed as a percentage of the estimated parameter, making it easier to compare the standard errors for estimates of different magnitudes.

$$\text{Err } \% = \frac{s(\hat{\theta}_j)}{\hat{\theta}_j} \tag{33}$$

Although the percentage measure can become inconvenient when $|\hat{\theta}|$ is very small, it is therefore recommended to use several metrics when analyzing system identification results.

Experimental Setup

This section describes the experimental setup and the experiments conducted to investigate the effects of icing on the performance of an electric UAV propeller system.

Data Acquisition

The experiments presented in this paper were conducted in an icing wind tunnel (IWT) at the VTT Technical Research Centre of Finland in Helsinki [27]. The test section of the IWT has a square shape with a $0.7\,\mathrm{m} \times 0.7\,\mathrm{m}$ opening. The IWT facility allows for testing at temperatures ranging from $-40\,^{\circ}\mathrm{C}$ to $25\,^{\circ}\mathrm{C}$ at wind speeds of up to $50\,\mathrm{m/s}$ and liquid water content (LWC) between 0 and $1.0\,\mathrm{g/m^3}$. The liquid water content is calibrated at the beginning of the test campaign with the ice accretion on a rotating cylinder [28]. A diagram showing the setup of the IWT is shown in figure Fig. 3.

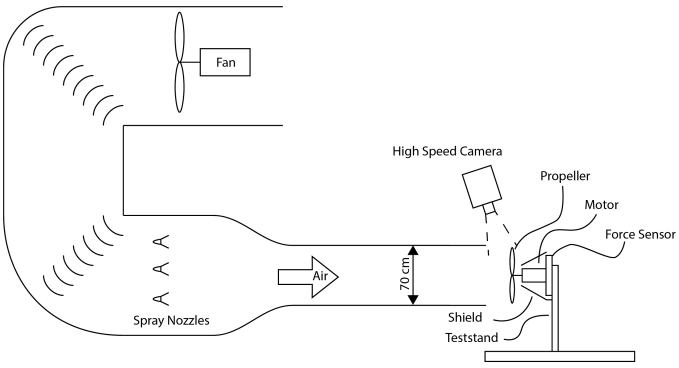

Figure 3: An illustration of the wind tunnel at the VTT in Helsinki. Source [17].

A series 1780 test stand from Tyto Robotics [29] was used to perform the propeller experiment and log data. The test stand allowed for logging at 40 Hz of the following data: input PWM signal, supply current and voltage, optical motor velocity, propeller torque, and propeller thrust forces. The test stand uses the standard 50 Hz PWM protocol to generate the input signal to the ESC [30], where the possible input PWM values are in the range [1000,2000]µs, where 1000 µs is equivalent to no power, and 2000 µs is full throttle. The propeller used in the experiments is the "Propeller 21x13 CCW 2B E" manufactured by Mejzlik Propellers s.r.o., which has a radius of $D = 0.53\,\mathrm{m}$ and, accordingly, sweeps an area of $S_p = 0.22\,\mathrm{m}^2$.

The motor selected for the experiments is the Axi 5345 HD 3D Extreme V2 — a star-connected 3-phase BLDC motor. The motor was controlled using a Kontronik JIVE Pro 80+ HV Brushless ESC, operated in mode 3, which doesn't auto-calibrate the throttle range on start-up and uses a pre-selected setup, i.e. [1000,2000]µs.

The phase voltage generated by the ESC was logged separately from the supply voltage using the Analog Discovery 2, a digital oscilloscope capable of logging true RMS AC voltage data at a 10 Hz sampling rate. Furthermore, based on Eq. 9, the phase voltage measurement also makes it possible to compute the phase current.

JavaScript was used to generate various input signals through the Tyto Robotics software. In particular — multistep, sawtooth, and chirp signals were generated to drive the motor in an open loop configuration while the sensor data was recorded.

Experiment Design

The experiments were conducted on two separate occasions. The first set of experiments involved no-load calibration tests and was conducted in a workshop environment. The second set of experiments dedicated to system identification was performed in the icing wind tunnel at VTT.

No-load Experiments

Prior to IWT tests, no-load experiments were performed to test the scripts used to generate input PWM throttle commands and to test the logging equipment.

During the no-load experiments, it was discovered that based on the motor datasheet and the power supply, the measured voltage $v_{l\text{-}l}$ was much lower than expected. Therefore, a voltage measurement calibration was performed to solve this discrepancy using the motor speed constant $k_V = 195$ (RPM/V) acquired from the motor datasheet [31]. The constant k_V relates the input phase voltage to the motor shaft speed of the motor in no-load conditions, i.e., $i \approx 0$,

$$\omega(t) = k_V \cdot v(t) \quad , \quad \text{assuming zero load.} \tag{34}$$

Based on the motor shaft speed, the measured line-to-line voltage, and the known k_V constant, the phase voltage was calibrated such that Eq. 34 was satisfied. Leading to the following corrected definition based on Eq. 14,

$$v(t) = 3.073 \frac{v_{l\text{-}l,measured}(t)}{\sqrt{3}} \tag{35}$$

Post-experiment analysis of the equipment suggests that the digital oscilloscope might require active differential voltage probes to measure PWM-modulated AC voltage accurately. Nonetheless, the measured data has been deemed useful as the goal of this paper is primarily to identify the effect of icing on the identified model parameters and not to find the exact value of each parameter. The described k_V-calibration is therefore deemed an acceptable pre-processing of the measured voltage data in the context of this paper. The calibration result is presented in Figs. 4 and 5. In addition, Figure 4 shows the alignment of the calibrated voltage measurement with the motor shaft speeds measurements in a no-load experiment, according to Eq. 34, and Fig. 5 demonstrates the non-linear relation between the PWM command and the input phase voltage.

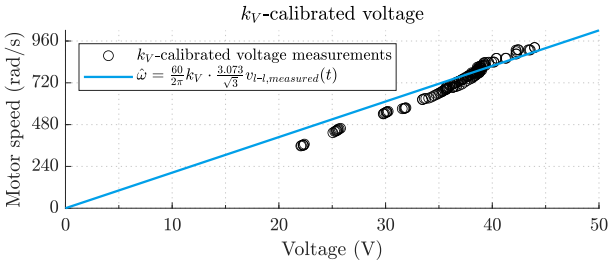

Figure 4: k_V-calibrated phase voltage plotted against motor shaft speed obtained from a no-load multistep experiment.

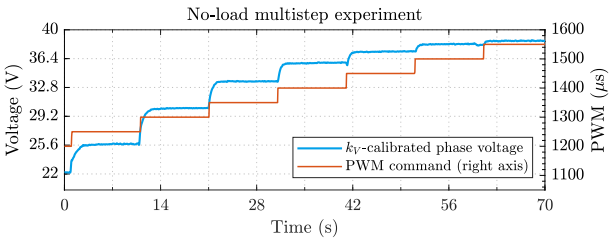

Figure 5: PWM command and the k_V-calibrated phase voltage obtained from a no-load multistep experiment.

Although the k_V-calibration is not significant for analyzing the change of electric model parameters due to icing, it does affect the uncertainty in phase current, which is calculated based on the voltage as shown in Eq. 9. This is especially important for the analysis of the identified motor-based torque model in the Results section.

IWT Experiments

A total of 22 system identification experiments were carried out at the IWT, comprising 18 steady-state multistep tests. Additionally, 11 ice accretion runs were performed to accrete the desired propeller ice shapes for each iced experiment. The ice accretion runs were performed at identical conditions, where the duration of the experiment, in the range {0,20,40,60}s, was the only variable used to influence the severity of the tested ice shapes. More about ice accretion runs is presented in section IWT Experiments — Ice Accretion. While the temperature significantly impacts the accreted ice and the resulting aerodynamic penalties, the primary objective of this paper is not to describe the penalties associated with a specific ice shape. Instead, the purpose is to evaluate the sensitivity of various model parameters in an electric propulsion system model to icing. Thus, the results are deemed valid even when only one temperature is considered. The complete experiment plan is presented in Table 1.

Table 1: Experiments performed at the IWT

Test	PWM input	Airspeed	Ice accretion	Repeated
1-2	Multistep	20 m/s	no ice	x2
3-6	Multistep	25 m/s	no ice	x4
7-9	Multistep	30 m/s	no ice	x3
10	Multistep	20 m/s	20 s	x1
11	Multistep	25 m/s	20 s	x1
12	Multistep	30 m/s	20 s	x1
13	Multistep	20 m/s	40 s	x1
14	Multistep	25 m/s	40 s	x1
15	Multistep	30 m/s	40 s	x1
16	Multistep	20 m/s	60 s	x1
17	Multistep	25 m/s	60 s	x1
18	Multistep	30 m/s	60 s	x1
23 [a]	Constant PWM	25 m/s	{20,40,60} s	x11

[a] Ice accretion runs. See flowchart in Fig. 9 for further explanation.

The multistep test was designed to cover the available PWM range [1000,2000]µs and allow all measured states to reach a steady state before each new step. In practice, this resulted in six equal PWM steps of 10 seconds each, from 1230 µs to 1530 µs as shown in Fig. 6. Although 1530 µs is far from full throttle, testing with higher values was difficult due to RPM saturation caused by power supply limitations. Nonetheless, the tests cover a wide range around the typical UAV trim speed of 4200 RPM.

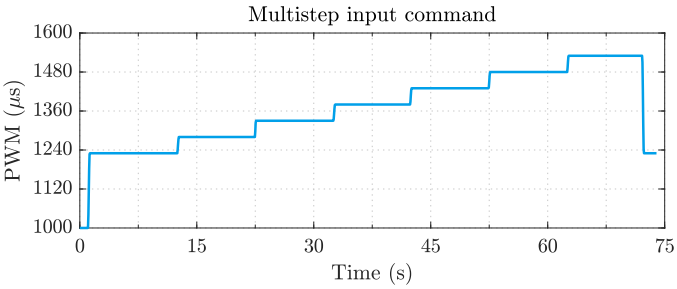

Figure 6: The figure shows the multistep input signal used to drive the motor in system identification experiments. The PWM signals are generated through a script in Tyto Robotics software and sent to ESC which drives the motor.

Selected data showing torque and thrust measurements from the multistep experiments is presented in Figs. 7 and 8. The data demonstrates a clear correlation between ice accretion and propeller performance. Specifically, as the ice exposure time increases, the torque of the propeller also increases while the thrust decreases. Furthermore, the effect of airspeed, which increases both torque and thrust, can also be observed.

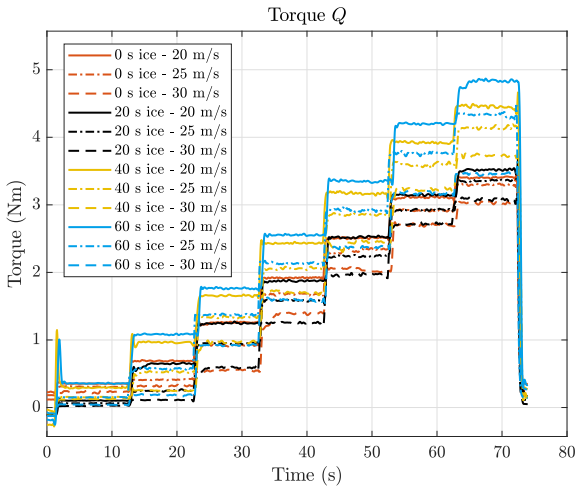

Figure 7: Torque measured during the performed multistep experiments.

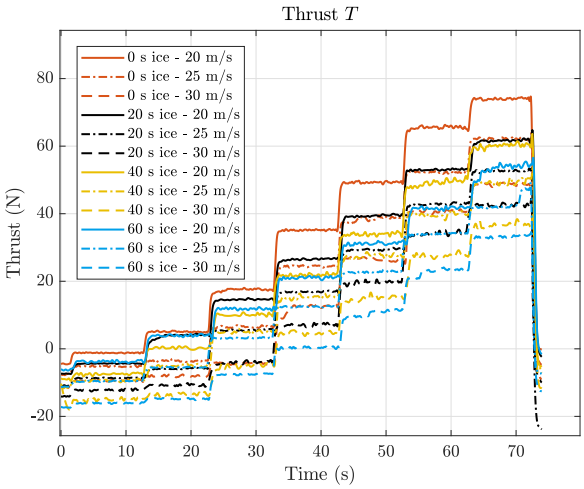

Figure 8: Thrust measured during the performed multistep experiments. The negative thrust values indicate the sections where the propeller is windmilling due to low RPM and non-zero airspeed.

IWT Experiments — Ice Accretion

The experiments conducted in this study varied in two parameters, namely airspeed V_a and ice accretion time. The airspeed was tested in the range of 20 m/s to 30 m/s, which is a typical cruise speed range for small fixed-wing UAVs, while the ice accretion time was tested in the range of 0 to 60 s. The decision to limit the largest ice shapes to an accretion time of 60 s was based on the observation that in the tested conditions, ice shapes accreted for longer periods, e.g., 80 s, are prone to shedding during the multistep experiment. Although larger ice shapes can be accreted on the slower parts of the propeller, uneven ice shedding from the blade tips exacerbates the problem causing significant imbalance and propeller vibrations, which are highly undesirable [17]. Moreover, the air temperature has a significant impact on ice shedding time, with lower temperatures leading to more shedding. Based on ice shedding times and performance degradation results presented in [17], where the same propeller has been used, the test temperature of $-10\,^{\circ}$C was found to be optimal, i.e., resulting in the least ice shedding and highest performance degradation. The values of LWC and median volume diameter (MVD), shown in

Table 2, were selected based on the continuous maximum icing envelope defined in CFR 14, Part 25, Appendix C [32] within the capabilities of the IWT.

Table 2: Overview of the tested atmospheric icing conditions.

LWC	MVD	Air Temperature
$0.44\,\mathrm{g/m^3}$	$22.7\,\mu\mathrm{m}$	$-10\,^\circ\mathrm{C}$

The propeller was cleaned, and new ice was accreted before each iced experiment to ensure the consistency of the accreted ice shapes. Furthermore, to test the ice shape integrity, the iced propeller was commanded to 5700 RPM for 10 seconds to shed loose ice. If that happened, the propeller was cleaned, and the ice accretion process was repeated as indicated in the experiment flow chart in Fig. 9. In these ice-accretion runs, the accretion occurred at a constant atmospheric setting specified in Table 2, with the airspeed of $25\,\mathrm{m/s}$ and the propeller rotation rate of 4200 RPM. The only parameter that was changed to create the different ice shapes is the duration of the ice accretion, varying from $20\,\mathrm{s}$ to $40\,\mathrm{s}$ and $60\,\mathrm{s}$. Furthermore, the wind tunnel was switched on $30\,\mathrm{s}$ prior to the propeller experiments to enable the airflow to settle.

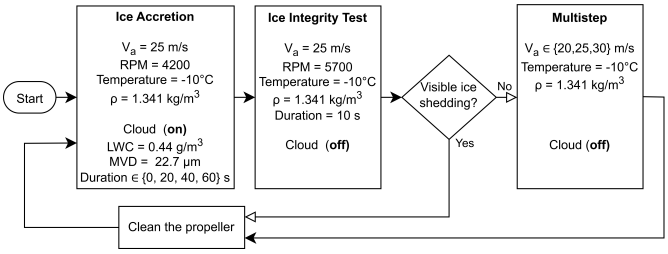

Figure 9: Flowchart for the IWT experiments.

To correctly identify the performance degradation of a propeller due to icing, the tested ice shapes had to be consistent throughout each experiment. Therefore, the ice accretion times were based on typical ice shedding times. In initial calibration runs, it was discovered that at $-10\,^\circ\mathrm{C}$, ice shedding was highly likely for ice shapes accreted for $80\,\mathrm{s}$ or more — a result consistent with findings in [17].

Figs. 10–12 show the accreted ice shapes before and after the multistep experiments. As shown in Table 1, three different ice shapes are accreted by varying exposure time to icing conditions, from 20 to 40 and $60\,\mathrm{s}$. The side-by-side comparison of the propeller blades with ice shapes highlights the degradation the ice shape experiences during a multistep test. Ideally, the ice should have the same shape throughout the whole experiment. However, as seen in the figures, some degradation can be observed near the tip of the blades and on the forward-facing surface of the blades, although the accreted ice on the leading edge is visually consistent.

The performance degradation due to the accreted ice shapes can be assessed by calculating the propeller efficiency throughout the experiments. Here the propeller efficiency is based on the measured thrust, torque, and motor shaft speed similar to Tyto Robotics calculation in [33]. In this paper, the calculated efficiency is also normalized by the ice-free efficiency to compare the effect of different ice shapes, resulting in the following formula,

$$\eta_p = \frac{T}{Q \cdot \omega} \cdot \left(\frac{T_{\text{clean}}}{Q_{\text{clean}} \cdot \omega_{\text{clean}}} \right)^{-1} \quad , \quad V_a \equiv V_{a_{\text{clean}}} \tag{36}$$

where the airspeed V_a is accounted for by calculating η_p based on clean and ice experiments performed at the same airspeed.

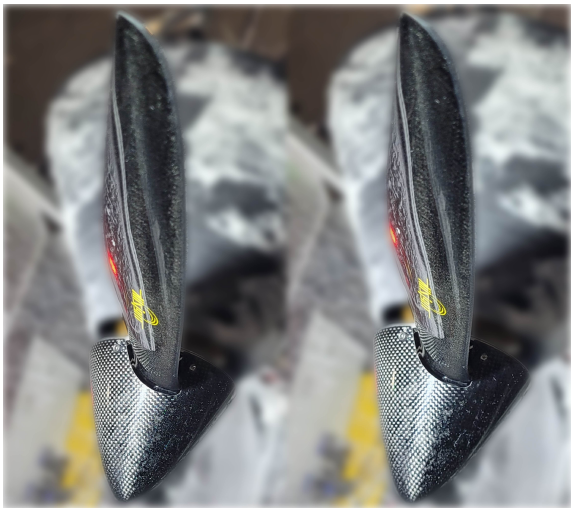

Figure 10: $20\,\mathrm{s}$ ice shape before (left) and after (right) the multistep experiment.

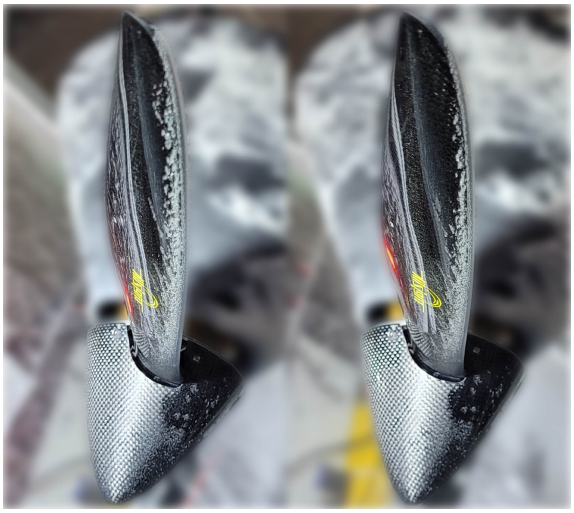

Figure 11: $40\,\mathrm{s}$ ice shape before (left) and after (right) the multistep experiment.

Figure 12: $60\,\mathrm{s}$ ice shape before (left) and after (right) the multistep experiment.

Figure 13 presents calculated propeller efficiencies using Eq. 36, indicating the reduction in efficiency for the tested ice shapes. It should be noted that the calculated efficiencies are not valid during the windmilling sections when the propeller does not produce propulsion force and a negative thrust is measured, as shown in Fig. 8. The valid efficiency results can therefore be observed from approximately 23 seconds onwards. The efficiency results clearly demonstrate an efficiency reduction of approximately 20%, 40%, and 50% for ice shapes accreted for 20, 40, and 60 s, respectively. Furthermore, in the context of multistep experiments, analyzing propeller efficiency is a useful method to investigate ice shape consistency. For instance, the sharp increase in efficiency observed after 33 seconds and 2 seconds before the end of the experiment with a 60 s ice shape is most likely due to ice shedding. Additionally, smaller ice-shedding events and gradual degradation of the ice shapes during the experiment could explain the gradual increase in propeller efficiency throughout the experiment. Some of the spikes in the calculated efficiencies can be explained by the misalignment of the time-series data in the clean and iced experiments, which is relevant because of the normalization performed in Eq. 36.

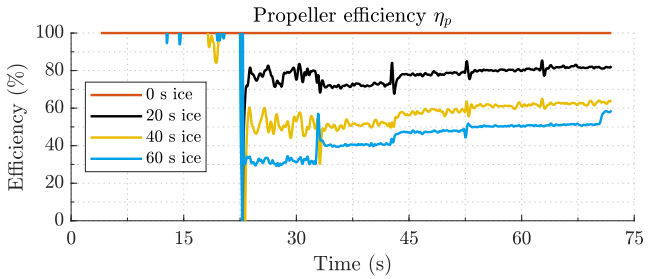

Figure 13: Propeller efficiency calculated using Eq. 36. The figure shows results for experiments performed at $V_a = 25\,\mathrm{m/s}$

Results

This section presents the identification results for each modeled UAV propulsion subsystem. The results are visualized using bar plots for parameter values and estimation confidence intervals, tables for estimation error metrics, and graphs displaying modeling results. The model for each subsystem is identified at four different icing severity levels, defined by ice accretion time from 0 to 60 s. The modeling and identification results are presented in the following order:

- Electrical Subsystem
- Mechanical Subsystem
- Aerodynamic Subsystem

Electrical Subsystem Identification

The initial input that enters the modeled propulsion system is the PWM throttle input. The PWM signal enters the ESC and controls how much of the available power supply voltage is made available to the phase voltage at the armature coils of the motor. The function that describes this relationship is the ESC transmission function $F_{\mathrm{ESC}}(\delta(t))$, which in this paper has been identified to be a 2$^{\mathrm{nd}}$-order function of the normalized PWM signal $\delta_t \in [0, 1]$, as shown in Eq. 8. The nonlinear relation between F_{ESC} and the input δ_t over the range covered by the multistep experiment is highlighted in Fig. 14. The prediction result based on the identified $\hat{F}_{\mathrm{ESC}}(\delta_t)$ polynomial is shown in the figure as well, demonstrating a good fit in the tested range. The coefficients of the identified polynomial are given in Table 3 and visualized in Fig. 15.

Table 3: Identified ESC transmission function parameters.

$$F_{ESC}(\delta_t) = p_0 + p_1 \cdot \delta_t + p_2 \cdot \delta_t^2$$

Model		$\hat{\theta}$	$s(\hat{\theta})$	Err %	RMSE	R^2
0 s ice	p_0 (-)	1.27e-05	1.39e-07	1.1 %	.0106	.989
	p_1 (-)	0.00235	2.58e-05	1.1 %		
	p_2 (-)	−1.80e-06	6.19e-08	3.5 %		
20 s ice	p_0 (-)	1.35e-05	2.12e-07	1.6 %	.0097	.990
	p_1 (-)	0.00249	3.91e-05	1.6 %		
	p_2 (-)	−2.08e-06	9.30e-08	4.5 %		
40 s ice	p_0 (-)	1.36e-05	2.47e-07	1.8 %	.0104	.988
	p_1 (-)	0.00250	4.57e-05	1.8 %		
	p_2 (-)	−2.07e-06	1.09e-07	5.3 %		
60 s ice	p_0 (-)	1.35e-05	2.80e-07	2.1 %	.0117	.985
	p_1 (-)	0.00250	5.19e-05	2.1 %		
	p_2 (-)	−2.06e-06	1.24e-07	6.0 %		

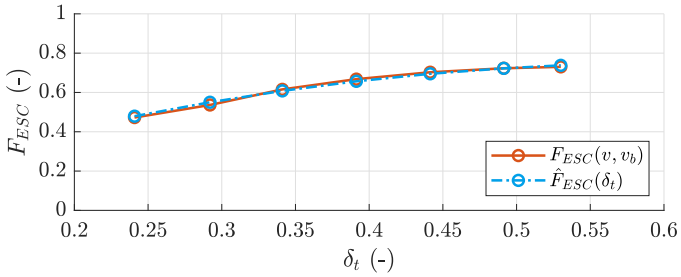

Figure 14: Relation between F_{ESC} and δ_t during a multistep experiment performed at $V_a = 25\,\mathrm{m/s}$ with a 20 s ice shape. The $F_{\mathrm{ESC}(v,v_b)}$ is calculated using Eq. 7, while the $\hat{F}_{\mathrm{ESC}}(\delta_t)$ is given by the identified 2$^{\mathrm{nd}}$-order polynomial from Table 3.

As seen in Fig. 15, the identified $F_{\mathrm{ESC}}(\delta_t)$ parameters do not change significantly as a function of icing severity. This makes sense as the change of load on the motor, caused by accreted ice, should not change the behavior of the voltage transmitted through the ESC. One can, however, notice a slight difference between the parameters obtained for the clean case compared to the iced cases. This sensitivity can be noticed in several of the identified models.

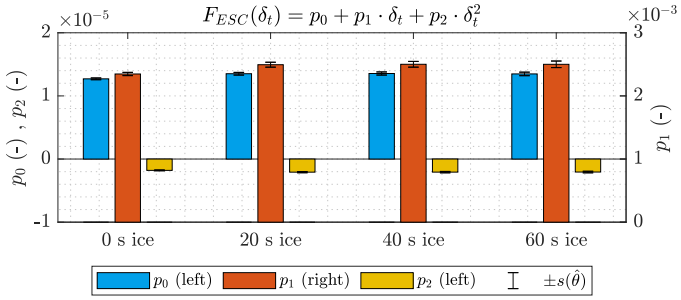

Figure 15: $F_{\mathrm{ESC}}(\delta_t)$ polynomial identified at four icing levels.

One of the hypotheses to explain the observed deviation in the ice-free case is related to the fact that ice-free experiments were performed at the start of the testing day and before the IWT chamber was humified, although all other conditions were maintained throughout the testing day. Mixing experiment types throughout the day could have mitigated this problem.

Figures 16 and 17 show F_{ESC}-based prediction results for phase voltage and phase current.

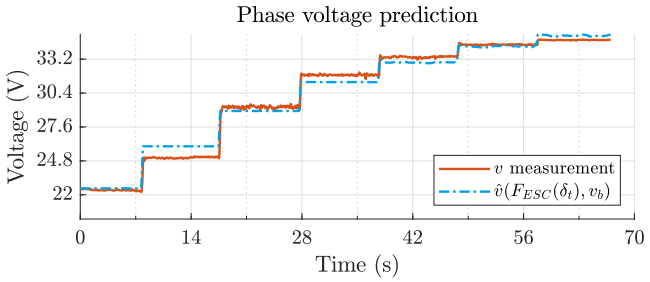

Figure 16: Phase voltage from a multistep experiment performed at $V_a = 25\,\mathrm{m/s}$ with a 20 s ice shape. The F_{ESC} based prediction is given by Eq. 6.

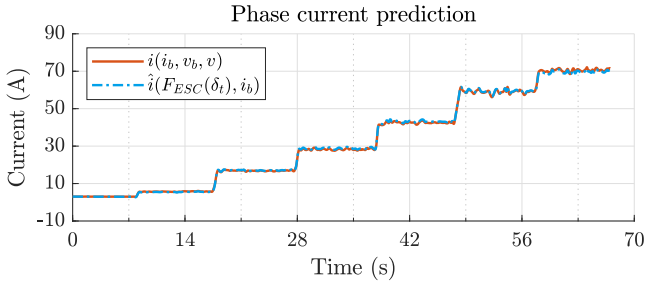

Figure 17: Phase current obtained from a multistep experiment performed at $V_a = 25\,\mathrm{m/s}$ with a 20 s ice shape. The reference phase current is calculated as shown in Eq. 9, while the F_{ESC} based prediction is given by Eq. 10.

Motor Shaft Velocity Model

Having identified the ESC transmission function, the next model in the line is given by voltage balance in the equivalent circuit, which relates phase current i and voltage v to the motor shaft speed ω as shown in Eq. 11.

As discussed in the theory and experiment setup sections, identifying a voltage balance model for the equivalent ESC and BLDC motor circuit has been challenging. The modeling challenges can, in part, be related to the k_V-compensation performed for the phase voltage resulting in increased uncertainty in the calculated phase current, as well as to the nonlinear dynamics introduced by the ESC. Nonetheless, given the available data, the identification attempts of a linear 1st-order model show that model parameters are time-varying and change with system states. It was therefore decided that the data-sheet value of the electrical motor resistance R in [31] should be used to simplify the identification process.

Figure 18 shows identification attempts of the model in Eq. 12 using different partitions of the test data. In the upper subplot, the whole experiment is used, while in the lower subplot, one model is identified based on the first half of the experiment, and a second model is identified based on the last half.

The model identified using the first half of the experiment, presented in Fig. 19, has a comparably small bias, v_0, and a back-EMF constant k_E consistent with the motor data-sheet value of $k_V = 195$ (RPM/V), as shown in Eq. 37.

$$k_V = \frac{1}{k_E} \quad , \quad k_E = 0.046\,\frac{\mathrm{V}}{\mathrm{rad\,s}} \Rightarrow k_V = 208\,\frac{\mathrm{RPM}}{\mathrm{V}} \tag{37}$$

Furthermore, the difference between the smallest and largest k_E values is 3% of its magnitude which is smaller than the computed standard error, as seen in Table 4. In contrast, the models identified based on the last half and the whole experiment have larger biases and are inconsistent with the data-sheet value for k_V. Nonetheless, the most useful outcome of voltage balance modeling is that according to the experiment data, the rate of conversion of mechanical energy to electrical through the back-EMF constant does not change significantly as a function of icing, except for the slight deviation in the ice-free case, which has been mentioned earlier.

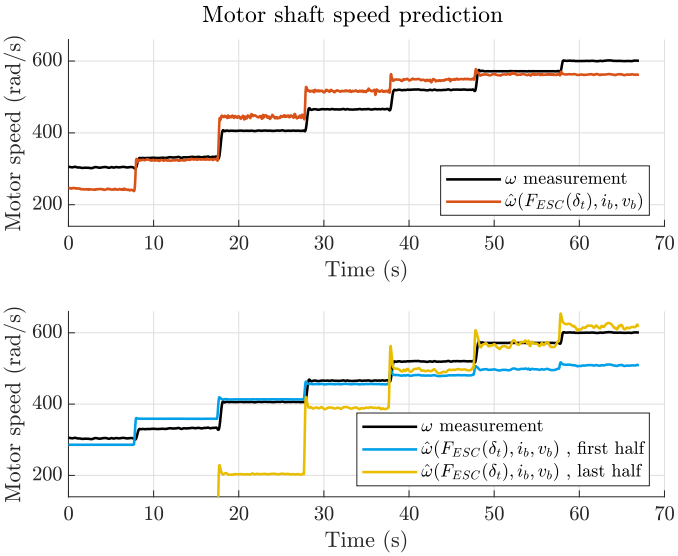

Figure 18: Motor shaft speed prediction based on Eq. 12 where phase voltage is computed using $\hat{F}_{\mathrm{ESC}}(\delta_t)$ as in Eq. 6. The upper subplot shows the result of a model identified based on the whole experiment, while the lower subplot shows the results of models identified using the first and last halves of the experiment.

Table 4: Voltage balance model identified based on the first half of the multistep experiments with a predetermined R.

$$v\,(t) = Ri\,(t) + k_E\omega\,(t) + v_0$$

Model		$\hat{\boldsymbol{\theta}}$	$\boldsymbol{s(\hat{\theta})}$	Err %	RMSE	$\mathbf{R^2}$
0 s ice	v_0 (V)	8.39	1.75	20.9 %	1.32	.782
	$R\,(\Omega)$	.0340	N/A	N/A		
	$k_E\,(\frac{\mathrm{V}}{\mathrm{rad/s}})$	.0464	.00472	10.2 %		
20 s ice	v_0 (V)	9.20	1.64	17.9 %	1.10	.891
	$R\,(\Omega)$	.0340	N/A	N/A		
	$k_E\,(\frac{\mathrm{V}}{\mathrm{rad/s}})$	.0462	.00427	9.2 %		
40 s ice	v_0 (V)	9.29	1.40	15.1 %	0.92	.925
	$R\,(\Omega)$	.0340	N/A	N/A		
	$k_E\,(\frac{\mathrm{V}}{\mathrm{rad/s}})$	.0471	.00370	7.9 %		
60 s ice	v_0 (V)	9.20	1.24	13.4 %	0.72	.954
	$R\,(\Omega)$	.0340	N/A	N/A		
	$k_E\,(\frac{\mathrm{V}}{\mathrm{rad/s}})$	.0478	.00330	6.9 %		

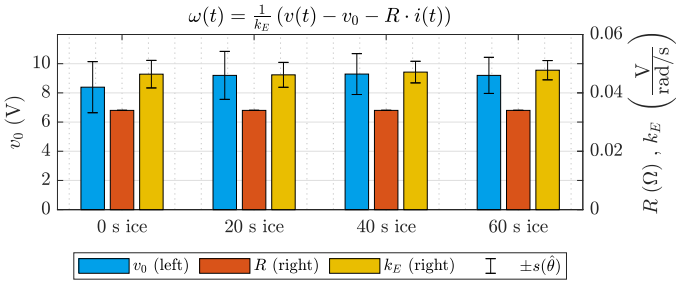

Figure 19: Voltage balance model parameters identified based on the first half of the multistep experiments at four icing levels, as presented in Table 4.

Mechanical Subsystem Identification

In steady-state operation, the mechanical subsystem given by Eq. 16 describes the relationship between the phase current i and the torque Q generated by the motor. During initial calibration tests, it has been discovered that the zero-load current i_0, which described the friction and losses in the no-load operation of the motor, is not constant and changes with the speed of the motor as shown in Fig. 20. Furthermore, the fact that the i_0 has a response curve similar to the phase current leads to collinear regressors in the formulation of an LS regression problem, complicating the identification process. As expected, direct use of the LS algorithm for system identification results in negative i_0 values, while the MATLAB's constrained solver `fmincon` [34] returns near-zero values of $i_0 < 1 \times 10^{-4}$. Due to this sensitivity, a decision was made to utilize the measurements from the zero-load experiments and set the i_0 to a constant value of 2.54 A, corresponding to the average value over the tested range; this value is also consistent with modeling results in [7]. The identified parameters with predetermined i_0 can be viewed in Fig. 21 and Table 5.

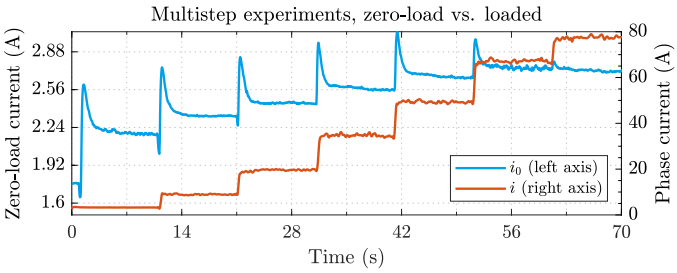

Figure 20: Zero-load current i_0 compared to loaded experiment current i, in a multistep experiment. The current values are calculated using Eq. 9.

Table 5: Mechanical torque model identified with predetermined i_0.

$$Q(t) = \text{bias} + k_Q \cdot (i(t) - i_0)$$

	Model	$\hat{\theta}$	$s(\hat{\theta})$	Err %	RMSE	R^2
0 s ice	bias (Nm)	.258	.0654	25.3%	.153	.985
	i_0 (A)	2.54	N/A	N/A		
	k_Q ($\frac{\text{N m}}{\text{A}}$)	.0466	.00209	4.5%		
20 s ice	bias (Nm)	.172	.0669	39.0%	.120	.990
	i_0 (A)	2.54	N/A	N/A		
	k_Q ($\frac{\text{N m}}{\text{A}}$)	.0490	.00217	4.4%		
40 s ice	bias (Nm)	.341	.0846	24.8%	.151	.988
	i_0 (A)	2.54	N/A	N/A		
	k_Q ($\frac{\text{N m}}{\text{A}}$)	.0568	.00256	4.5%		
60 s ice	bias (Nm)	.279	.1133	40.6%	.242	.972
	i_0 (A)	2.54	N/A	N/A		
	k_Q ($\frac{\text{N m}}{\text{A}}$)	.0571	.00240	4.2%		

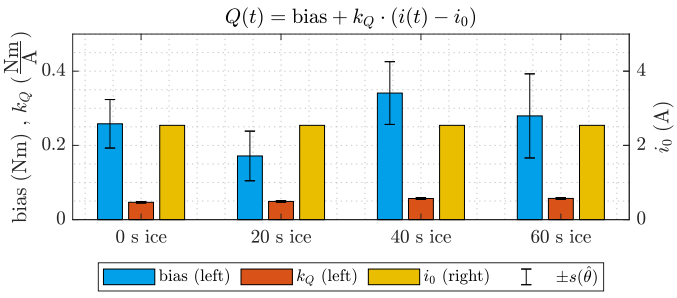

Figure 21: Visualization of the motor-based torque model parameters presented in Table 5.

The second parameter in the motor-based model is the torque parameter k_Q, which increases by 23% from the ice-free case to the most severely iced case according to the model identification results. This is, however, not consistent with the identified back-EMF, which in theory should be equal to k_Q but was determined to be constant for all tested ice shapes. The average magnitude of both k_E and k_Q is very similar, 0.0469 vs. 0.0523; however, their sensitivity to ice accretion is not. This can be related to the previously discussed uncertainty in the phase current data, calculated using the k_V-calibrated phase voltage measurements as shown in Eq. 9. Moreover, it should be noted that the model presented in Table 5 may be incomplete since it neglects any dynamic losses that occur during the conversion of electrical energy to mechanical energy. To account for this, an attempt was made to incorporate the viscous friction term $c_v\omega$ into the regression process. However, as mentioned in the Methods section, the resulting value of c_v was less than 10^{-7}. The identified bias in Table 5, which accounts for about 3% to 6% of the model output, might be explained by the uncertainty in the phase current data, the unmodeled losses, and measurement noise.

Aerodynamic Subsystem Identification

In this section, propeller torque and thrust are modeled and analyzed.

Propeller Torque Model

When studying the torque from the motor's perspective, as in the previous section, the produced torque is directly related to the current drawn by the motor. However, this approach does not consider what kind of load is present on the motor shaft. Another way of modeling torque in propeller systems is to use the airspeed, motor shaft speed, and propeller characteristics, including diameter and swept area, as described in section Aerodynamic System. The equation describing this relationship is presented in Eq. 23, and the identified coefficients are presented here in Fig. 22 and Table 6. As shown in Table 6 the model does not have a constant bias term. Identification of a polynomial with a near-zero bias was achieved by applying the SVD-based LS algorithm described in section System Identification, where the reduced SVD solution was used in the regression process. Although the parameters fit the model better, the use of the reduced SVD solutions renders the parameter uncertainties provided by the standard error invalid in the propeller torque model.

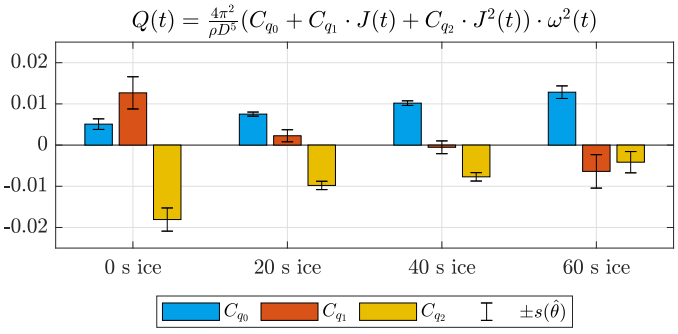

Figure 22: Visualization of the aerodynamic torque model presented in Table 6.

Analysis of the aerodynamic torque coefficients shows an interesting relation between ice accretion and the identified torque models. The torque coefficients exhibit a change that follows a trend from the ice-free to the most severely iced case. The torque curves in Fig. 23 provide a visualization of the change in torque coefficient as a function of ice accretion duration where an increase in C_Q of approximately 16% can be observed from the ice-free case to the most severely iced case.

Table 6: Identified aerodynamic torque model coefficients. The standard errors presented in this table should be analyzed cautiously as model identification results were obtained using the reduced SVD solution in the regression process, which impacts the calculated parameter uncertainties.

$$Q(t) = \frac{4\pi^2}{\rho D^5}(C_{q_0} + C_{q_1} \cdot J(t) + C_{q_2} \cdot J^2(t)) \cdot \omega^2(t)$$

Model		$\hat{\theta}$	$s(\hat{\theta})$	Err %	RMSE	R^2
0 s ice	C_{q_0}	.0051	.0013	25.3 %	0.107	.973
	C_{q_1}	.0127	.0039	30.8 %		
	C_{q_2}	−.0181	.0028	15.6 %		
20 s ice	C_{q_0}	.0075	.0005	6.6 %	0.036	.997
	C_{q_1}	.0023	.0015	64.5 %		
	C_{q_2}	−.0098	.0010	10.3 %		
40 s ice	C_{q_0}	.0103	.0006	5.5 %	0.041	0.996
	C_{q_1}	−.0005	.0016	290.5 %		
	C_{q_2}	−.0077	.0010	13.2 %		
60 s ice	C_{q_0}	.0128	.0015	11.9 %	0.119	.974
	C_{q_1}	−.0064	.0041	63.6 %		
	C_{q_2}	−.0042	.0026	62.2 %		

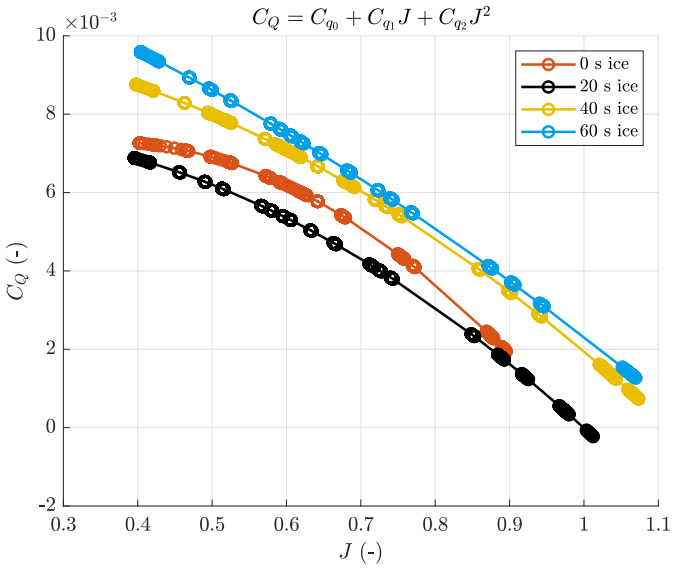

Figure 23: Nondimensionalized torque predictions based on the aerodynamic torque polynomial Eq. 21 identified at four icing severity levels. Each curve in the figure is obtained from an average of three experiments, each performed with ice shapes of the same severity but at three different airspeeds: $V_a \in \{20, 25, 30\}$m/s.

Overall, the torque curves in Fig. 23 demonstrate a clear pattern of increasing torque with longer ice accretion times. However, one can also see that the curves for the ice-free experiments and those with ice shapes accreted for 20 s stand out as outliers. A closer examination of the motor shaft speed and torque measured during these experiments, shown in Fig. 24, reveals that the motor shaft speed in the ice-free case is lower compared to the iced case, while the torque remains relatively constant. The torque data is as expected since the amount of ice accreted after 20 s is very small, as shown in Fig. 10. However, the comparably low motor speed measured in the ice-free case is physically inconsistent as, typically, the increased drag due to ice would slow down the propeller, and the clean propeller should be faster than the iced propeller given the same throttle input. Further analysis of the propeller efficiency for these two cases reveals that the clean propeller is more efficient, as shown in Fig. 25. This means that the measured clean propeller thrust is significantly higher compared to the iced propeller thrust and that the measured motor speed in the clean case could be incorrect. It is suspected that this discrepancy in motor shaft speed measurements is due to the fact that the ice-free experiments were performed at the start of the testing day and before the IWT chamber was humidified, while the other experiments were conducted later in the day. Nonetheless, more validation data is required to confirm this hypothesis. Furthermore, since the experiments were grouped based on ice accretion times, there may be measurement bias between the grouped experiments, a fact that will be considered in future experiments. Despite this discrepancy, a holistic analysis of the torque curves in Fig. 23 reveals a clear increasing trend in torque as a function of ice accretion time, which is consistent with similar findings reported in [17].

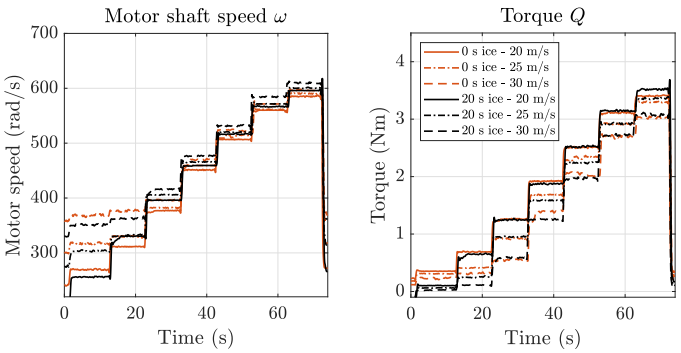

Figure 24: Motor shaft speed and torque measurements from the ice-free and 20 s ice shape experiments. The motor shaft speed in the ice-free case is lower compared to the iced case, while the torque remains relatively constant.

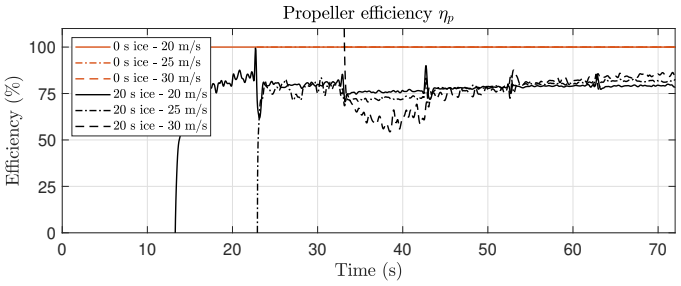

Figure 25: The figure shows propeller efficiencies for the 20 s ice shape experiments normalized by the propeller efficiencies from the ice-free experiments, calculated using Eq. 36. The efficiency of the iced propeller is clearly lower in the iced case by around 25%.

Torque predictions based on the nondimensionalized torque coefficient C_Q and the current-based model are presented in Fig. 26.

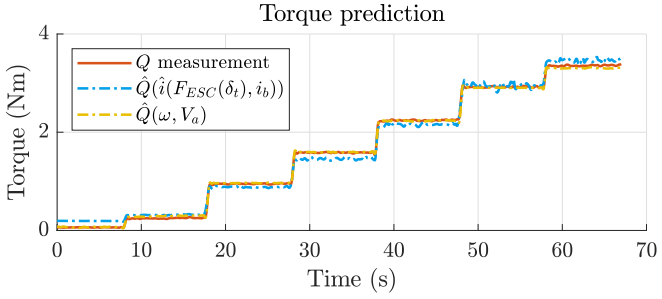

Figure 26: Torque during a multistep experiment performed at $V_a = 25$ m/s with 20 s ice shape. The prediction results are based on two models. The motor-based model is given in Table 5 with the phase current computed using $\hat{F}_{\text{ESC}}(\delta_t)$ as in Eq. 10. The aerodynamic torque model is based on the advance ratio polynomial in Table 6.

As prediction results in Fig. 26 indicate, both models can produce meaningful predictions across the whole range of the experiment. However, a closer comparison of prediction error metrics in Tables 5 and 6 shows that the aerodynamic torque model outperforms the motor-based model, with an RMSE ratio of approximately 1:2 on average. The relatively poor fit of the motor-based model can be attributed to the issues with the zero-load current, the unmodeled losses, and the fact that the phase current is obtained indirectly through voltage measurements as shown in Eq. 9. Nonetheless, both models can be encoded in a simulation framework to simulate the effect of icing on a UAV propeller system, both from the motor side and the aerodynamic side.

Propeller Thrust Model

Similarly to torque, thrust can be modeled as a function of advance ratio, motor shaft speed, and propeller geometry. The identification results are presented in Fig. 27 and Table 7. The curves can be seen in Fig. 28. Similarly to the torque curves, the thrust curves change due to icing. Visually comparing the change in C_Q curves and C_T curves might indicate that the change in C_T curves is less significant; however, a percent-wise comparison reveals a reduction by 40% on average from the ice-free case to the most severely iced case, which is much larger than the 16% change observed in the C_Q curves. Furthermore, similarly to the aerodynamic torque model, the aerodynamic thrust model was identified using the reduced SVD solution in the regression algorithm to get near-zero bias terms. Consequently, this invalidated the parameter uncertainties provided by the standard errors in Table 7.

Table 7: Identified aerodynamic thrust model coefficients. The standard errors presented in this table should be analyzed cautiously as model identification results were obtained using the reduced SVD solution in the regression process, which impacts the calculated parameter uncertainties.

$$T(t) = \frac{4\pi^2}{\rho D^4}(C_{t_0} + C_{t_1} \cdot J(t) + C_{t_2} \cdot J^2(t)) \cdot \omega^2(t)$$

Model		$\hat{\theta}$	$s(\hat{\theta})$	Err %	RMSE	R^2
0 s ice	C_{t_0}	.1170	.0035	3.0%	0.806	.998
	C_{t_1}	−.0516	.0104	20.1%		
	C_{t_2}	−.1020	.0072	7.1%		
20 s ice	C_{t_0}	.1070	.0095	8.9%	1.219	.995
	C_{t_1}	−.0860	.0274	31.9%		
	C_{t_2}	−.0590	.0187	31.8%		
40 s ice	C_{t_0}	.1160	.0189	16.4%	2.675	.977
	C_{t_1}	−.1240	.0523	42.2%		
	C_{t_2}	−.0302	.0342	13.2%		
60 s ice	C_{t_0}	.0990	.0067	6.7%	1.013	.996
	C_{t_1}	−.0903	.0186	20.6%		
	C_{t_2}	−.0448	.0121	27.0%		

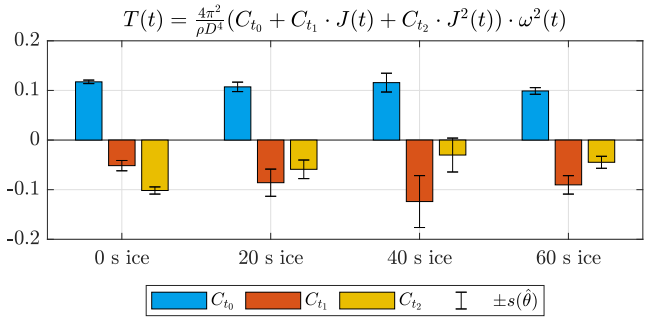

Figure 27: Visualization of the aerodynamic thrust model presented in Table 7.

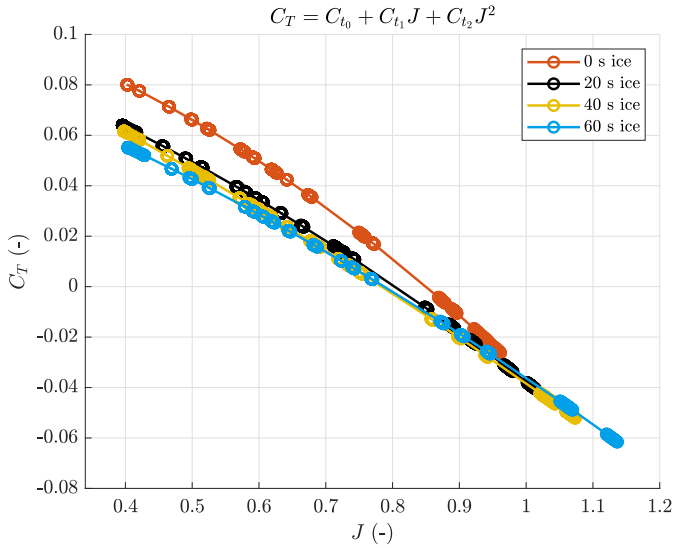

Figure 28: Nondimensionalized thrust predictions based on the aerodynamic thrust polynomial Eq. 20 identified at four icing severity levels. Each curve in the figure is obtained from an average of three experiments, each performed with ice shapes of the same severity but at three different airspeeds: $V_a \in \{20, 25, 30\}\mathrm{m/s}$.

Analysis of the torque and thrust curves in Figs. 23 and 28 reveals that ice accretion on the propeller impacts both torque and thrust. However, when comparing the percentage change of C_Q and C_T caused by icing, it becomes evident that the thrust is significantly more affected than the torque. Thus, in terms of the propeller's efficiency given by Eq. 36, it can be concluded that, in the tested conditions, the decrease in thrust caused by icing is more detrimental than the increase in torque. This finding is useful for designing an icing detection system, as it sheds light on the sensitivity of torque and thrust to icing. Based on the presented results, an icing FDF based on thrust estimation is, therefore, more likely to generate accurate detection results than an icing FDF based on torque.

Throttle-based Thrust Model

A throttle-based thrust model allows for modeling the thrust as a function of throttle input, e.g., given by the normalized PWM input δ_t. As presented in section Throttle-based Thrust and Torque Models, the Beard & McLain model Eq. 24 has been tested. The identified model parameters are presented in Fig. 29 and Table 8. Figure 30 highlights the change of the motor coefficient k_m, which reduces by 12% from the ice-free case to the most severely iced case.

Table 8: Identified throttle-based thrust model parameters.

$$T_{BM} = \frac{1}{2}\rho S_p e_p((k_m \delta_t)^2 - V_a^2)$$

Model		$\hat{\theta}$	$s(\hat{\theta})$	Err %	RMSE	R^2
0 s ice	k_m ($\frac{\mathrm{m}}{\mathrm{s}}$)	91.152	2.845	3.1%	3.949	.977
	e_p (-)	0.2635	.0144	5.5%		
20 s ice	k_m ($\frac{\mathrm{m}}{\mathrm{s}}$)	86.813	2.473	2.9%	2.681	.986
	e_p (-)	0.2477	.0122	4.9%		
40 s ice	k_m ($\frac{\mathrm{m}}{\mathrm{s}}$)	83.372	2.664	3.2%	2.722	.985
	e_p (-)	0.2554	.0142	5.6%		
60 s ice	k_m ($\frac{\mathrm{m}}{\mathrm{s}}$)	80.943	1.022	1.3%	1.473	.994
	e_p (-)	0.2462	.0053	2.1%		

Thrust predictions based on the aerodynamic and the throttle-based thrust models are presented in Fig. 31. Comparison of prediction error metrics in Tables 7 and 8 shows that the aerodynamic thrust model

outperforms the throttle-based model, with an RMSE ratio of approximately 1:2 on average. In particular, the Beard & McLain model struggles at the start and end points of the experiment, indicating the possibility of unmodeled higher-order dependencies, which is expected for a simplified throttle-based model. The thrust models, much like the torque models, can prove valuable in simulating the impact of icing on the performance of UAV propeller systems. Furthermore, having torque and thrust models makes it possible to isolate the changes arising from alterations in motor shaft speed and UAV airspeed from icing-induced changes, which is highly relevant in the context of icing detection.

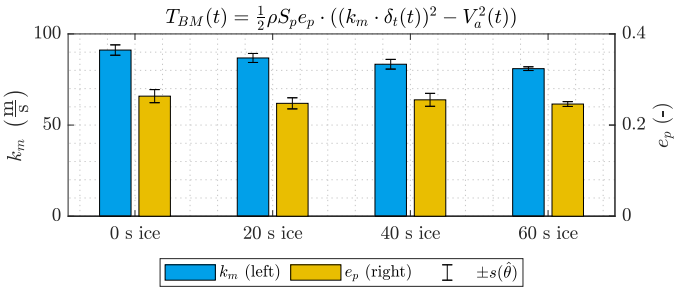

Figure 29: Visualization of the throttle-based thrust model presented in Table 8.

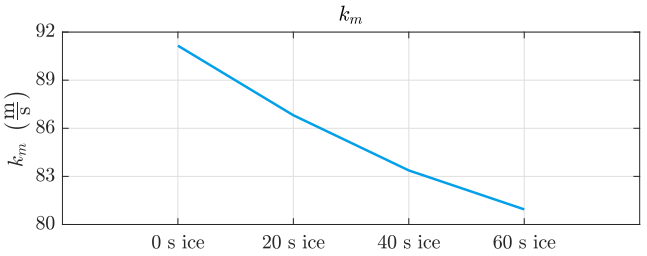

Figure 30: Thrust constant k_m in Eq. 24 identified at four icing levels.

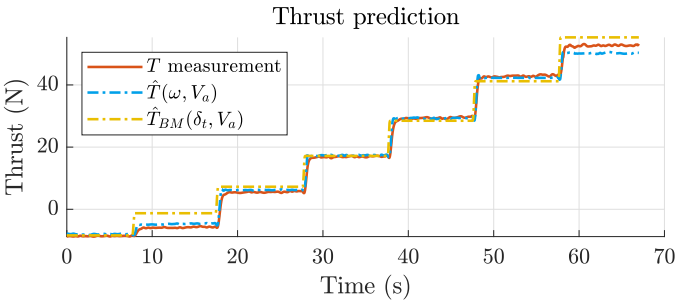

Figure 31: Thrust during a multistep experiment performed at $V_a = 25\,\mathrm{m/s}$ with 20 s ice shape. The prediction results are based on two models. The aerodynamic thrust model is based on the advance ratio polynomial in Table 7, while the throttle-based model is presented in Table 8.

Discussion

Several important findings and nuances related to identifying propulsion system models have been uncovered in the previous section. These are further commented on here.

The presented results make it clear that the k_V-compensation of the measured phase voltage, performed in the data pre-processing step, has affected the uncertainty related to the phase current data, making it challenging to analyze the validity of the identified motor-based torque model. Despite this, the identification results of the electric subsystem are considered valid, as the scaling of the voltage does not affect the identified change with respect to icing. Furthermore, the correctness of the identified voltage balance and the motor-based torque models is validated by the fact that the identified back-EMF constant k_E and torque constant k_Q are of similar magnitude.

Concerning propeller performance, the study shows that propeller efficiency is significantly reduced by icing through an increase in torque and a reduction in thrust. The results also indicate that several ways of modeling both torque and thrust can be used to achieve comparable prediction results. This includes the motor-based torque, throttle-based thrust, and aerodynamic torque and thrust models. However, the aerodynamic models outperform the other model by a ratio of 1:2 based on the prediction RMSE values as seen in Tables 5–8. Overall, these findings emphasize the importance of considering the impact of icing on the performance of electric UAV propulsion systems, particularly the effect on propeller torque and thrust, which change significantly and can therefore be used to develop ice detection algorithms.

The limitations of this study are mostly related to the small number of icing conditions that were taken into account. As a result, identifying an icing effect model for the aerodynamic coefficients, such as the Bragg model [35], has been challenging. Therefore, more data is needed to better understand how atmospheric icing impacts the aerodynamic coefficients and, ultimately, the propeller's performance. Furthermore, although the primary goal of determining the parameter and subsystem sensitivities to icing has been achieved, the generalizability of the results may be limited due to the small number of tested icing conditions. Future research would therefore benefit from considering a broader range of icing conditions.

Conclusion

Modeling and performance analysis of an electric propeller system suitable for fixed-wing UAVs has been performed with the help of an icing wind tunnel. In particular, performance degradation due to ice accretion on the propeller blades has been studied. The tested icing conditions include three different ice shapes accumulated for 20, 40, and 60 seconds in otherwise identical atmospheric conditions. In addition, ice-free experiments have been conducted to establish the nominal propulsion system performance.

The propulsion system's electrical, mechanical, and aerodynamic subsystems have been identified through LS regression, using the reduced SVD solution in some cases. In addition, the comprehensive set of model parameters identified for varying ice shape sizes makes it possible to study the parameter sensitivity to icing severity and thereby deduce how each of the identified subsystems is affected.

In conclusion, this study has provided valuable insights into the impact of icing on propeller efficiency in the tested conditions of $-10\,^{\circ}\mathrm{C}$, with LWC of $0.44\,\mathrm{g/m^3}$, MVD of $22.7\,\mu\mathrm{m}$ and airspeed of $25\,\mathrm{m/s}$. In particular, the results show that, on average, the thrust is reduced by 40%, while the torque is increased by 16%, in total, resulting in a propeller power efficiency reduction of 50% and up to 70% in the worst case. Furthermore, a substantial reduction of propeller power efficiency by 20% occurs after just 20 seconds of ice accretion. These findings suggest that a detection system based on propeller efficiency monitoring could be a good starting point for an icing detection algorithm. Furthermore, these modeling results can also be incorporated into simulation frameworks and help the rapid development and testing of realistic icing detection systems. Additionally, having torque and thrust models enables the isolation of

icing-induced changes from other changes arising from alterations in power supply, motor shaft speed, and UAV airspeed, which can be relevant for ice detection systems.

In the context of ice protection systems (IPS), the study's results can help design requirements for IPS by quantifying the energy cost of not activating an IPS. Moreover, the documented propeller power efficiency reduction due to icing can help optimize the use of anti-icing and de-icing IPS modes. Overall, this study contributes to the development of IPS for electric UAV propulsion systems and thus enhances the safety and performance of UAVs in cold environments.

References

1. H. Shakhatreh, A. H. Sawalmeh, A. Al-Fuqaha, Z. Dou, E. Almaita, I. Khalil, N. S. Othman, A. Khreishah, and M. Guizani, Unmanned Aerial Vehicles (UAVs): A Survey on Civil Applications and Key Research Challenges *IEEE Access*, vol. 7, pp. 48572–48634, 2019.
2. S. Scheiermann, "MEMS sensors are the heart of a drone." `https://www.fierceelectronics.com/components/mems-sensors-are-heart-a-drone`, 2019. (Accessed on 20/03/2023).
3. R. Hann and T. A. Johansen, Unsettled Topics in Unmanned Aerial Vehicle Icing tech. rep., SAE Technical Paper, 2020.
4. Y. Cao, W. Tan, and Z. Wu, Aircraft Icing: An Ongoing Threat to Aviation Safety *Aerospace science and technology*, vol. 75, pp. 353–385, 2018.
5. C. Deiler and N. Fezans, Performance-based Ice Detection Methodology *Journal of Aircraft*, vol. 57, pp. 209–223, jan 2020.
6. R. M. McKillip, Algorithmic Icing Detection for eVTOL/AAM Aircraft in *AIAA AVIATION 2022 Forum*, p. 3963, 2022.
7. E. M. Coates, A. Wenz, K. Gryte, and T. A. Johansen, Propulsion System Modeling for Small Fixed-wing UAVs in *2019 International Conference on Unmanned Aircraft Systems (ICUAS)*, pp. 748–757, IEEE, 2019.
8. N. Michel, A. K. Sinha, Z. Kong, and X. Lin, Multiphysical Modeling of Energy Dynamics for Multirotor Unmanned Aerial Vehicles in *2019 International Conference on Unmanned Aircraft Systems (ICUAS)*, pp. 738–747, IEEE, 2019.
9. O. Moseler and R. Isermann, Application of Model-based Fault Detection to a Brushless DC Motor *IEEE Transactions on industrial electronics*, vol. 47, no. 5, pp. 1015–1020, 2000.
10. C. Xiang, X. Wang, Y. Ma, and B. Xu, Practical Modeling and Comprehensive System Identification of a BLDC Motor *Mathematical Problems in Engineering*, vol. 2015, 2015.
11. Y. Liu, L. Li, Z. Ning, W. Tian, and H. Hu, Experimental Investigation on the Dynamic Icing Process over a Rotating Propeller Model *Journal of Propulsion and Power*, vol. 34, no. 4, pp. 933–946, 2018.
12. Y. Liu, L. Li, W. Chen, W. Tian, and H. Hu, An Experimental Study on the Aerodynamic Performance Degradation of a UAS Propeller mMdel Induced by Ice Accretion Process *Experimental Thermal and Fluid Science*, vol. 102, pp. 101–112, 2019.
13. D. Kozomara, T. Neubauer, R. Puffing, I. Bednar, and W. Breitfuss, Experimental Investigation on the Effects of Icing on Multicopter UAS Operation in *AIAA AVIATION 2021 FORUM*, p. 2676, 2021.
14. P. Suurnäkki, M. Tiihonen, and T. Jokela, UAV Icing: Low Reynolds Number Drone Propeller Performance During Dynamic Icing Process in *AIAA AVIATION 2021 FORUM*, p. 2672, 2021.
15. A. Dhulipalla, N. Han, H. Hu, and H. Hu, A Comparative Study to Characterize the Effects of Adverse Weathers on the Flight Performance of an Unmanned-Aerial-System in *AIAA AVIATION 2022 Forum*, p. 3962, 2022.
16. E. Villeneuve, A. Samad, C. Volat, M. Béland, and M. Lapalme, Experimental Investigation of Icing Effects on a Hovering Drone Rotor Performance *Drones*, vol. 6, no. 11, p. 345, 2022.
17. N. C. Müller and R. Hann, UAV icing: A Performance Model for a UAV Propeller in Icing Conditions in *AIAA AVIATION 2022 Forum*, p. 3903, 2022.
18. I. Ozcer, D. Switchenko, G. S. Baruzzi, and J. Chen, Multi-shot Icing Simulations with Automatic Re-meshing tech. rep., SAE Technical Paper, 2019.
19. N. Müller, R. Hann, and T. Lutz, UAV Icing: Numerical Simulation of Propeller Ice Accretion in *AIAA AVIATION 2021 FORUM*, p. 2673, 2021.
20. R. Isermann, *Fault-diagnosis Systems: An Introduction from Fault Detection to Fault Tolerance*. Springer Science & Business Media, 2005.
21. O. M. Haaland, A. Wenz, K. Gryte, R. Hann, and T. Johansen, Detection and Isolation of Propeller Icing and Electric Propulsion System Faults in Fixed-Wing UAVs in *2021 International Conference on Unmanned Aircraft Systems (ICUAS)*, pp. 377–386, IEEE, 2021.
22. J. Wallisch and R. Hann, UAV Icing: Experimental Investigation of Ice Shedding Times with an Electrothermal De-Icing System in *AIAA AVIATION 2022 Forum*, p. 3905, 2022.
23. J. Zhao and Y. Yu, Brushless DC Motor Fundamentals Application Note AN047 Rev. 1.0, MPS, July 2014.
24. B. M. Simmons, System Identification for Propellers at High Incidence Angles *Journal of Aircraft*, vol. 58, no. 6, pp. 1336–1350, 2021.
25. R. W. Beard and T. W. McLain, *Small Unmanned Aircraft: Theory and Practice*. Princeton university press, 2012.
26. E. A. Morelli and V. Klein, *Aircraft System Identification: Theory and Practice*, vol. 2. Sunflyte Enterprises Williamsburg, VA, 2016.
27. M. Tiihonen, T. Jokela, L. Makkonen, and G.-J. Bluemink, VTT Icing Wind Tunnel 2.0 in *Winterwind International Wind Energy Conference*, 2016.
28. S. International, ARP5905 Calibration and Acceptance of Icing Wind Tunnels *Aerospace Recommended Practice ARP5905*, sep 2015.
29. Tyto Robotics, "Series 1780: Drone test stand - Tyto Robotics." `https://www.tytorobotics.com/pages/series-1780`, September 2020. (Accessed on 27/11/2022).
30. Tyto Robotics, "PWM signal troubleshooting - Tyto Robotics." `https://www.tytorobotics.com/blogs/testing-troubleshooting-guidelines/pwm-signal`, September 2020. (Accessed on 11/26/2022).

31. Model motors s.r.o., “AXI 5345/16 HD 3D EXTREME V2 KV195.” `https://www.modelmotors.cz/product/detail/514/`. (Accessed on 27/02/2023).

32. R. K. Jeck, Icing Design Envelopes (14 CFR Parts 25 and 29, Appendix C) Converted to a Distance-Based Format tech. rep., FAA technical center Atlanta City NJ, 2002.

33. T. Robotics, “How to measure brushless motor and propeller efficiency — tytorobotics.com.” `https://www.tytorobotics.com/blogs/articles/how-to-measure-brushless-motor-and-propeller-efficiency`. (Accessed on 11/03/2023).

34. The MathWorks, Inc., fmincon 2023. (Accessed on 20/03/2023).

35. M. Bragg, T. Hutchison, and J. Merret, Effect of Ice Accretion on Aircraft Flight Dynamics in *38th Aerospace Sciences Meeting and Exhibit*, p. 360, 2000.

Contact Information

Bogdan Løw-Hansen,
Email: bogdan.l.hansen@ntnu.no

Richard Hann,
Email: richard.hann@ntnu.no

Acknowledgments

We thank UBIQ Aerospace for providing access to the propeller test stand and VTT for assistance with the icing wind tunnel experiments. The work is partly sponsored by the Research Council of Norway through the following project code: 223254 and 316425.

Definitions/Abbreviations

BLDC	brushless direct current
CFD	computational fluid dynamics
DC	direct current
EMF	electromotive force
ESC	electronic speed controller
FDF	fault detection filter
IPS	ice protection systems
IWT	icing wind tunnel
LS	least squares
LWC	liquid water content
MEMS	micro-electromechanical system
MVD	median volume diameter
PWM	pulse-width modulation
RMSE	root-mean-square error
RPM	revolutions per minute
SVD	singular value decomposition
UAV	unmanned aerial vehicle

APPENDIX A: Additional model prediction results and experiment data

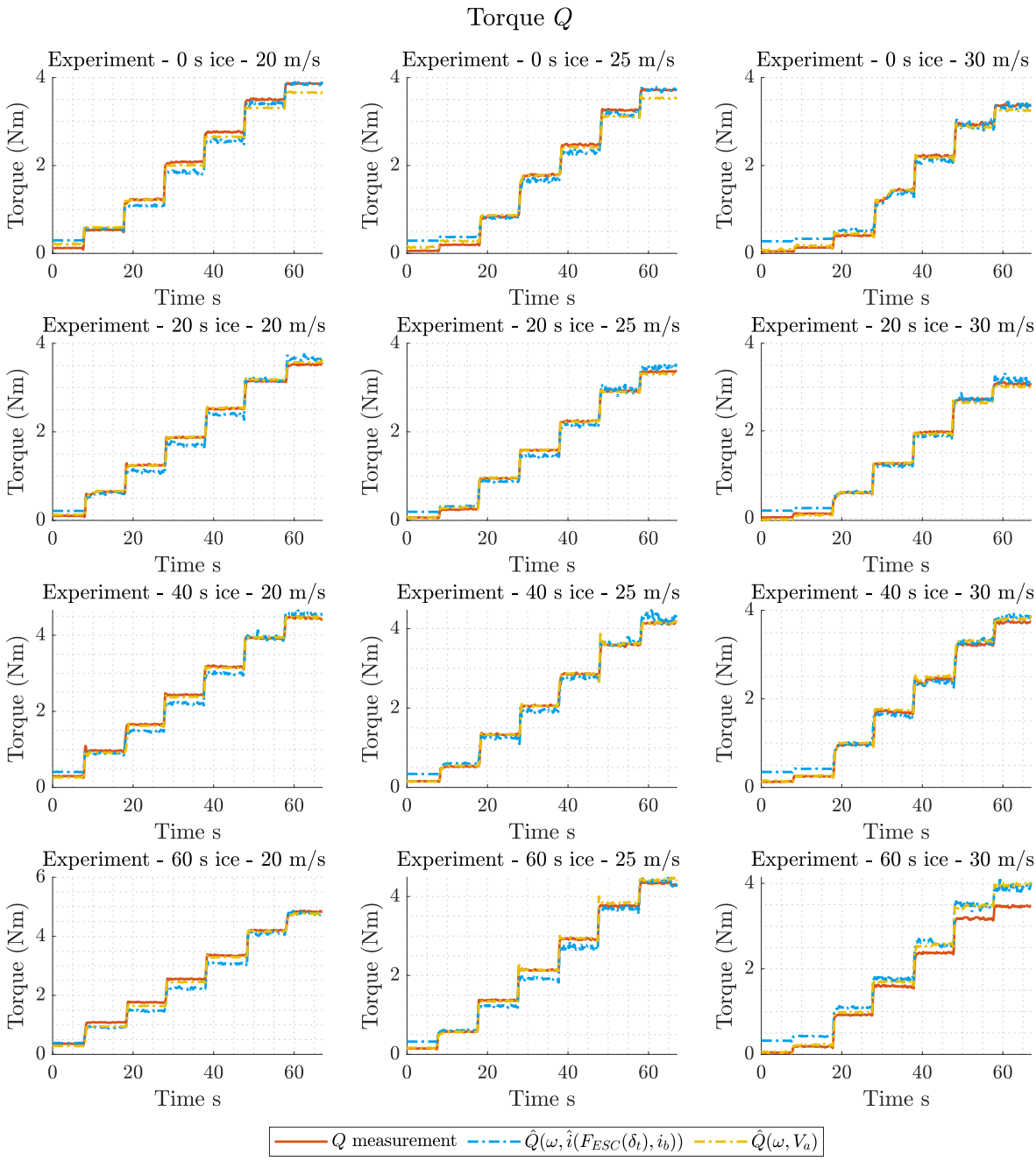

Figure 32: Torque during multistep experiments. The prediction results are based on two models. The motor-based model is given in Table 5 with the phase current computed using $\hat{F}_{\mathrm{ESC}}(\delta_t)$ as in Eq. 10. The aerodynamic torque model is based on the advance ratio polynomial in Table 6.

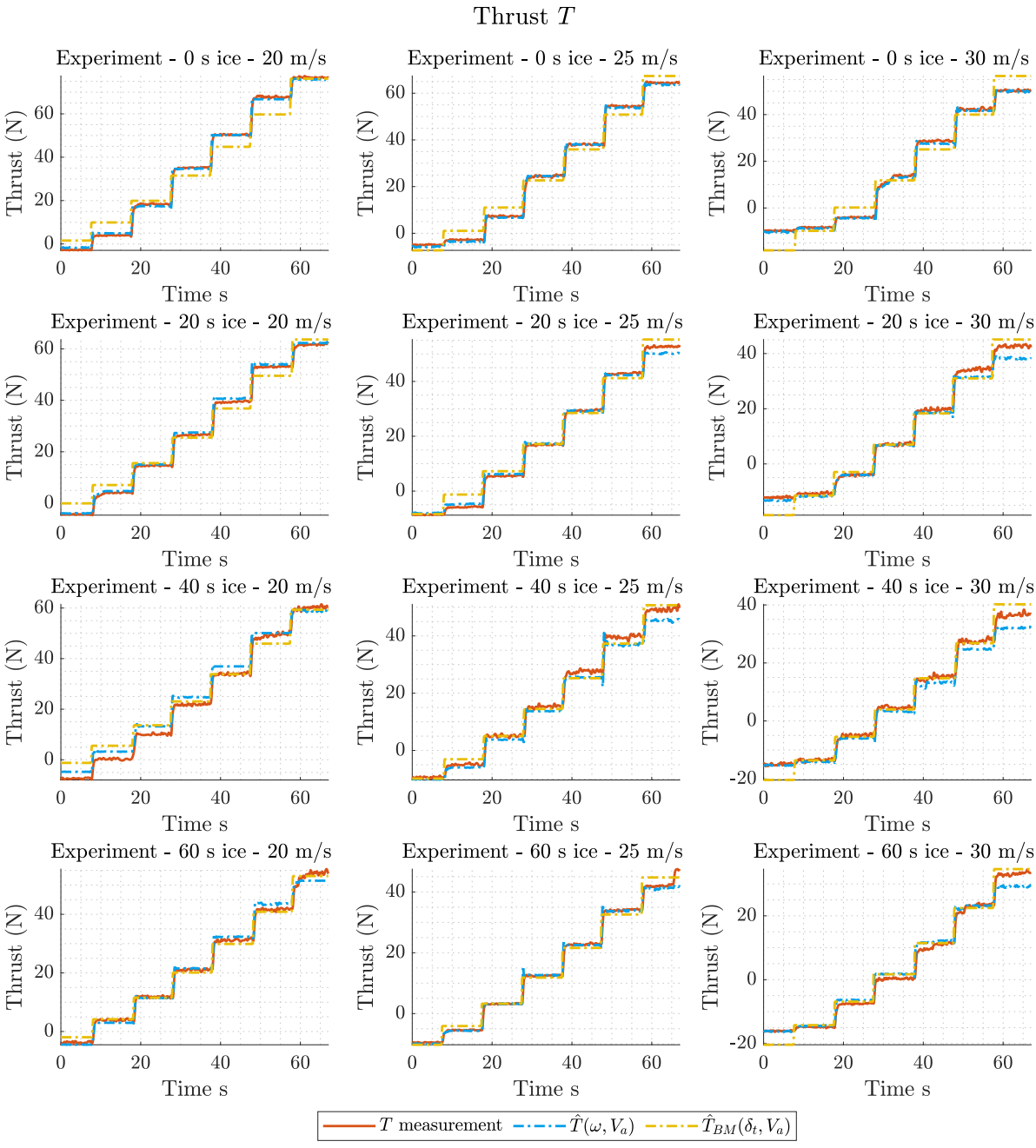

Figure 33: Thrust during multistep experiments. The prediction results are based on two models. The aerodynamic thrust model is based on the advance ratio polynomial in Table 7, while the throttle-based model is presented in Table 8.

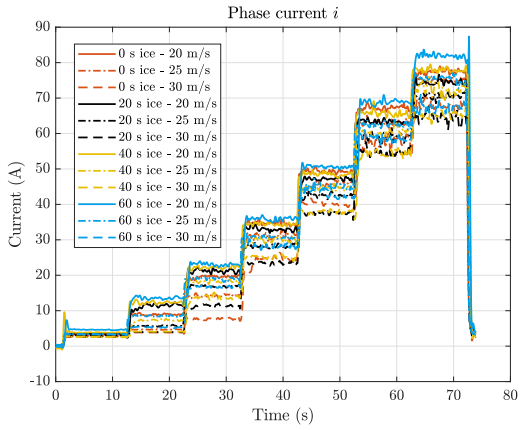

Figure 34: Phase current obtained from the performed multistep experiments. The phase current values were calculated as shown in Eq. 9.

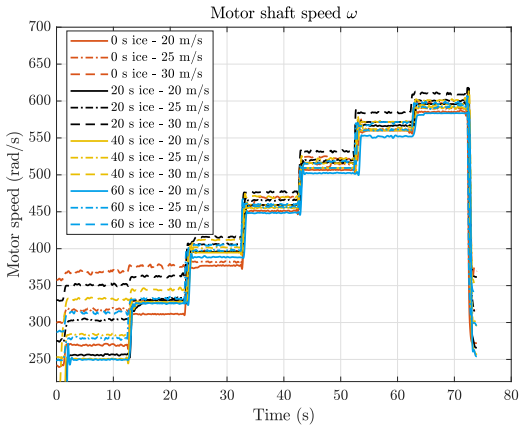

Figure 35: Motor speed measured during the performed multistep experiments.

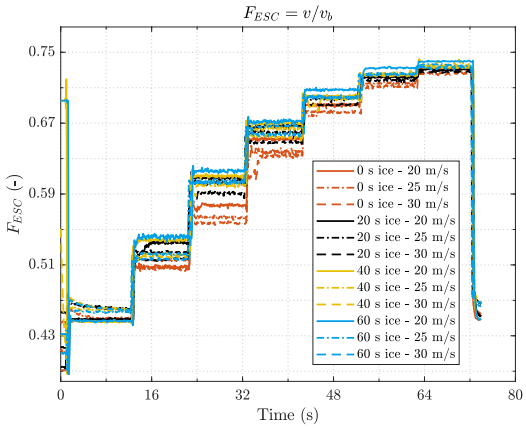

Figure 36: Mesured $F_{ESC}(v, v_b)$ obtained from the performed multistep experiments. The $F_{ESC}(v, v_b)$ values were calculated as shown in Eq. 7

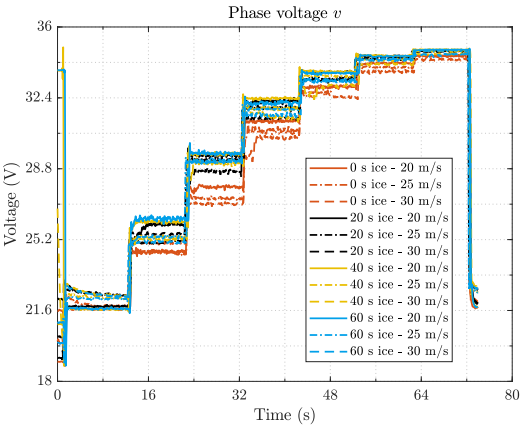

Figure 37: Phase voltage measured during the performed multistep experiments.

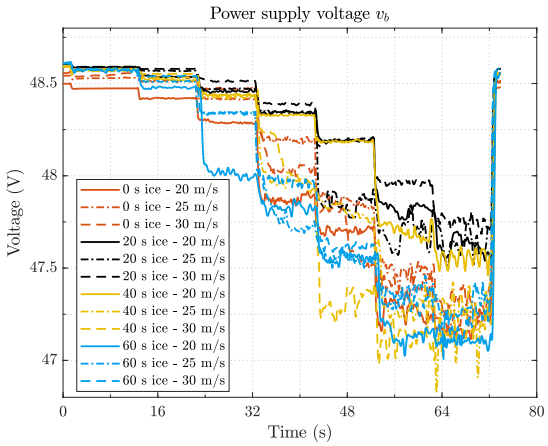

Figure 38: Power supply voltage obtained from the performed multistep experiments.